REGENERATION

Selective promotion of sensory innervation–mediated immunoregulation for tissue repair

Kaicheng Xu[1,2,3,4]†, Kaile Wu[1,2,3,4]†, Liang Chen[1,2,3,4]†, Yubin Zhao[1,2,3,4], Hengyuan Li[1,2,3,4], Nong Lin[1,2,3,4], Zhaoming Ye[1,2,3,4], Jianbin Xu[1,2,3,4]*, Donghua Huang[1,2,3,4]*, Xin Huang[1,2,3,4]*

Sensory innervation triggers the regenerative response after injury. However, dysfunction and impairment of sensory nerves, accompanied by excessive inflammation impede tissue regeneration. Consequently, specific induction of sensory innervation to mediate immunoregulation becomes a promising therapeutic approach. Herein, we developed a cell/drug-free strategy to selectively boost endogenous sensory innervation to harness immune responses for promoting tissue rehabilitation. Specifically, a dual-functional phage was constructed with a sensory nerve–homing peptide and a β-subunit of nerve growth factor (β-NGF)–binding peptide. These double-displayed phages captured endogenic β-NGF and localized to sensory nerves to promote sensory innervation. Furthermore, regarding bone regeneration, phage-loaded hydrogels achieved rapid sensory nerve ingrowth in bone defect areas. Mechanistically, sensory neurotization facilitated M2 polarization of macrophages through the Sema3A/XIAP/PAX6 pathway, thus decreasing the M1/M2 ratio to induce the dissipation of local inflammation. Collectively, these findings highlight the essential role of sensory innervation in manipulating inflammation and provide a conceptual framework based on neuroimmune interactions for promoting tissue regeneration.

INTRODUCTION

Peripheral nervous system regulates tissue development, homeostasis, and repair (*1*). It influences the regeneration processes, likely through the secretion of neural-related molecules or the differentiation of stem/precursor-like cells (*2*), and nerve depletion impairs tissue healing outcomes (*3*). The peripheral nerves can be divided into several categories, and they perform different functions in tissue repair. For example, overactivated sympathetic nerves trigger negative regenerative events (*4*), whereas sensory innervation contributes more to tissue healing. Numerous studies have shown that sensory nerves promoted adipose tissue regeneration (*5*), bone healing (*6*), and skin repair after ultraviolet-induced damage (*7*). However, the biological mechanism underlying sensory nerve–mediated tissue repair remains unclear, and there is currently no inductive strategy that specifically facilitates sensory innervation in regenerative medicine.

Sensory innervation detects and responds to environmental harmful stimuli, such as inflammatory mediators, mechanical damage, and intense heat in tissues, including skin, bone, and muscles, following acute injury (*8*). It relays signals to the immune system and directly affects immune cell function via neurotransmitters and neuropeptides (*9*), thus actively enhancing pathogen resistance and reducing inflammation (*10*, *11*). For instance, sensory neurons mediate immune responses by inhibiting cell recruitment, accelerating cell death, and enhancing efferocytosis of neutrophils, monocytes, and macrophages in mice (*12*). Therefore, it is reasonable to speculate that sensory innervation facilitates tissue repair, probably through the regulation of immunity.

After injury, inflammation immediately triggers a series of immune responses (*13*). Physiological inflammatory responses protect against harmful stimuli and restore the function of damaged tissues (*14*). However, excessive inflammation disrupts the microenvironment, resulting in the overexpression of pro-inflammatory cytokines, excessive production of reactive oxygen species (*15*), and disordered sensory innervation (*15*, *16*). This dysregulation of the sensory nerves, in turn, aggravates the inflammatory response, resulting in delayed tissue healing (*17*). Thus, the functional protection and promotion of sensory innervation, a key endogenous driver of neuronal immunoregulation, are promising components for tissue regenerative treatment.

Nerve tissues are abundant in the metabolically active regions of bone tissues (*18*), in which the regeneration outcome is substantially modulated by the immune system (*19*); therefore, in this study, we conducted relevant proof-of-concept research in the context of bone defects. We aimed to determine whether sensory innervation can manipulate the progression of local inflammation and subsequently affect tissue regeneration. Specifically, we constructed a double-displayed bacteriophage to function as double-sided adhesive tape, capturing autogenous nerve growth factors and localizing to local sensory fibers. This dual-functional treatment system specifically promoted sensory nerve ingrowth and regulated macrophage-mediated inflammatory responses in the microenvironment (Fig. 1). Mechanistically, we found that sensory nerves secrete semaphorin 3A (Sema3A) to downregulate the expression of XIAP, which further mediates the ubiquitination of PAX6 to facilitate macrophage polarization. Overall, our study aimed to selectively promote sensory innervation–mediated immunoregulation after acute injury, and these findings provide a promising strategy to use these neuroimmune interactions to promote tissue repair.

RESULTS

Sensory denervation is accompanied by inflammatory outburst

To determine the potential roles and mechanisms of sensory nerves in bone healing, the rates of spontaneous healing of rat mandibular defects with and without dissection of inferior alveolar nerve (IAN),

---

[1] Department of Orthopedic Surgery, The Second Affiliated Hospital, Zhejiang University School of Medicine, Hangzhou, Zhejiang, China. [2] Orthopedics Research Institute of Zhejiang University, Hangzhou, Zhejiang, China. [3] Key Laboratory of Motor System Disease Research and Precision Therapy of Zhejiang Province, Hangzhou, Zhejiang, China. [4] Clinical Research Center of Motor System Disease of Zhejiang Province, Hangzhou, Zhejiang, China.

*Corresponding author. Email: huangxinzeyy@zju.edu.cn (X.H.); huangdonghua@zju.edu.cn (D.H.); xu9709426@zju.edu.cn (J.X.)

†These authors contributed equally to this work.

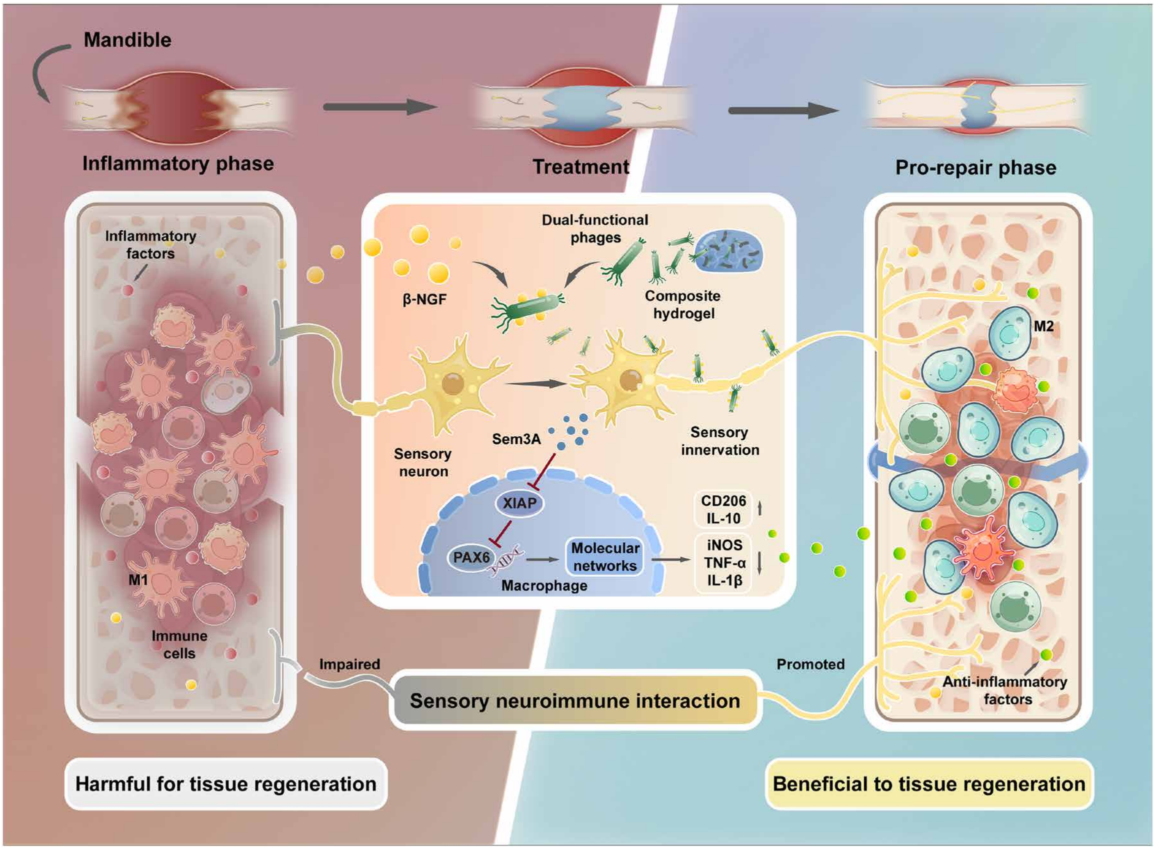

Fig. 1. Schematic illustration. The promoted bone regenerative processes induced by dual-functional phage-loaded composite hydrogels, progressed with selective promotion of sensory innervation and regulation of immune responses via neuroimmune interactions. The phages released from the hydrogel capture the autogenous β-NGF in the impaired microenvironment and home to local sensory nerve fibers to facilitate sensory innervation. The sensory neurons subsequently mediate macrophage polarization toward M2 phenotype through the Sema3A/XIAP/PAX6 pathway, which further induces the dissipation of local inflammation and improved bone healing outcome. β-NGF, β subunit of nerve growth factor; M1 and M2, M1 and M2 polarized macrophage.

also known as simple sensory nerve fibers (*20*), were compared (Fig. 2, A and B). The diameter of the mandibular defect was set at 4 mm to allow for spontaneous bone healing.

First, microcomputed tomography (micro-CT) was conducted to assess the defect repair effects at 2 and 8 weeks after transection of IAN (Fig. 2C). The sham group showed an increase in new bone tissue covering the defect area from 2 to 8 weeks, indicating healing potential. However, almost no new bone tissue was formed at any time point after denervation of IAN (Fig. 2, D and E). The quantitative micro-CT results further validated these observations. The defect coverage percentages were 2.77 ± 1.17 and 3.06 ± 1.07% at 2 and 8 weeks after denervation, respectively, which were much lower than those of the control (13.84 ± 1.39 and 67.25 ± 4.01%, respectively) (Fig. 2, F and G). The volume of newly formed bone in the denervated defect was significantly reduced at all time points (Fig. 2, F and G). Hematoxylin and eosin (H&E) and Masson staining histological analyses also showed almost no new bone formation in the defect area after 8 weeks of denervation (fig. S4, A and B). Immunohistochemical staining for alkaline phosphatase (ALP) and osteocalcin (OCN), which are indicators of the early and late stages, respectively, of osteogenic capacity further revealed the impaired bone regeneration outcome after IAN transection (fig. S4A). The ALP$^+$ and OCN$^+$ percentages in the sham group were both about twice as high as those in the denervation group (fig. S4C). In addition, tartrate-resistant acid phosphatase (TRAP) staining and immunofluorescence staining of CD31 were performed as well for evaluating bone resorption and vascularization during bone repair, respectively. The number of TRAP$^+$ cells more than tripled after 8 weeks of denervation, indicating the overactivated osteoclastic activity (fig. S5A). However, the expressed fluorescence intensity of CD31 after denervation was notably decreased, suggesting an impaired angiogenesis effect caused by IAN transection (fig. S5B). Together, these results indicated that the capacity for spontaneous endogenous bone repair, both in the early and late stages of injury, was remarkably delayed in the absence of sensory nerves. Consistently, sensory denervation impairing tissue repair has been observed in various tissues, including skin, muscle, and cornea. For instance, in the skin and muscle, the selective ablation of GINIP$^+$ somatosensory neurons delays wound closure and impairs muscle regeneration (*7*, *12*). In the cornea, sensory nerve disruption hinders tissue repair (*21*). In the context of bone tissue, Zhang *et al.* reported that the trabecular volume of rats was notably reduced by capsaicin-induced sensory neuron lesions (*22*).

Considering that active nerve growth mainly occurs during the early stage after injury (*23*), transcriptome sequencing was conducted to investigate the potential pathophysiological changes in the bone defect areas after sensory denervation for 1 week. The results of Pearson's correlation analysis suggested acceptable specimen

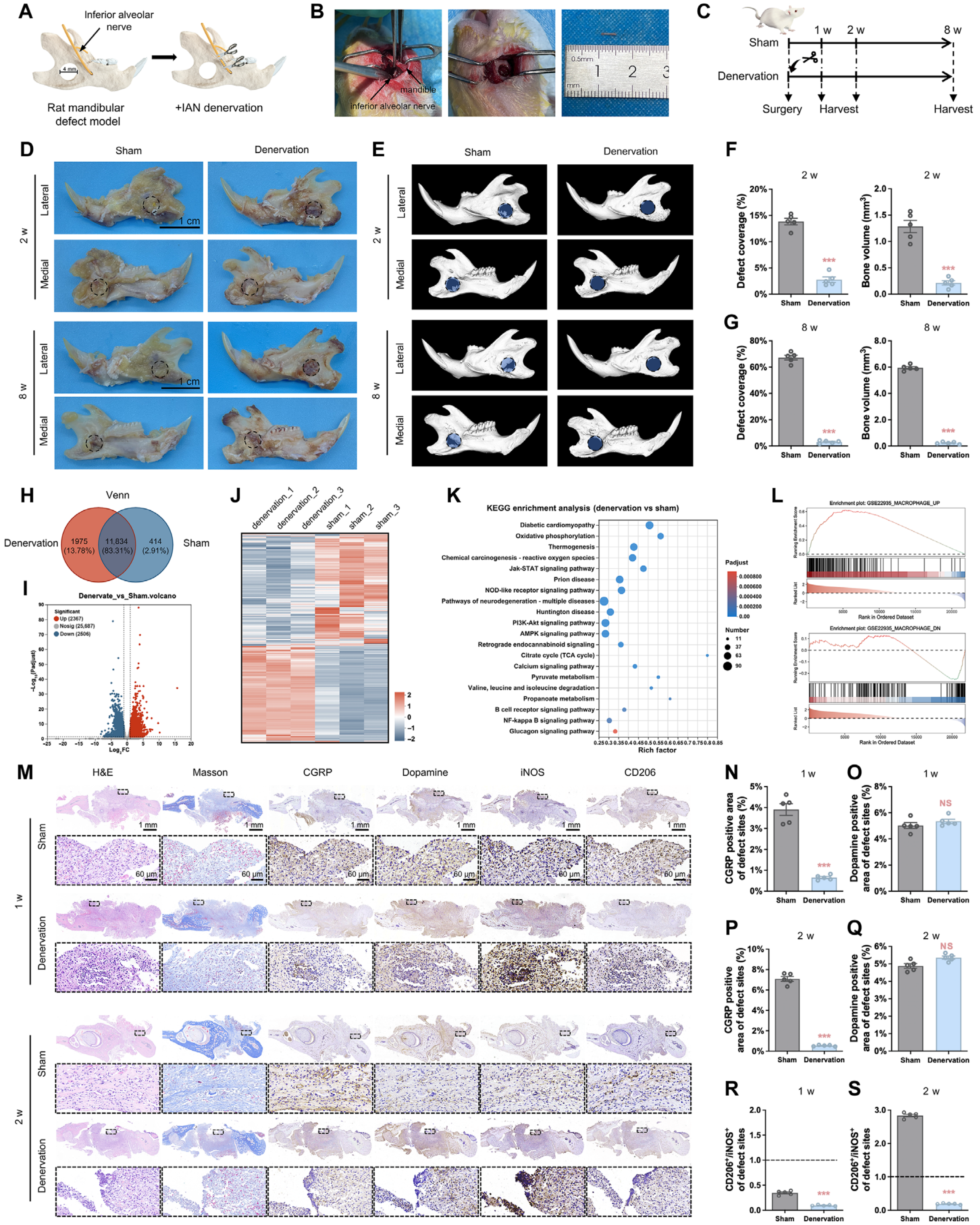

Fig. 2. Sensory denervation impairs bone healing after injury with aggravation of the inflammatory response. (**A** and **B**) Schematic representation of the rat mandibular defect and IAN innervation models. (**C**) Time durations of the animal experiments. w, weeks. (**D**) Photographs of mandibular samples and (**E**) the corresponding 3D reconstruction micro-CT images after 2 and 8 weeks of surgery. The black dotted circles in mandible photographs and the blue circles in reconstructed images represent the initial defect areas (diameter = 4 mm). Scale bars, 1 cm. (**F** and **G**) Quantitative analysis of coverage percentage and new bone volume at the defect site. (**H**) Venn diagram of the numbers of DEGs in the denervation and sham groups. (**I**) Volcano plot of differential gene expression between the two groups. (**J**) Heatmap of differential gene expression in the denervation and sham groups. (**K**) Enriched KEGG pathways in the denervation and sham groups. (**L**) GSEA of up-regulated and down-regulated macrophage-related genes. (**M**) Panoramic and partially enlarged images of H&E, Masson, and immunohistochemical stained tissues (for CGRP, dopamine, iNOS, and CD206) at 1 and 2 weeks after surgery. Scale bars, 1 mm and 60 μm, respectively. (**N** to **P**) Corresponding semiquantitative results of immunohistochemistry analysis at 1 week and (**Q** to **S**) 2 weeks after surgery. $***P < 0.001$; NS, not significant.

stability in the two groups (denervation versus sham; fig. S1A). Pronounced changes in transcript levels were observed (Fig. 2, H and I), as well as in the levels of differentially expressed genes (DEGs) (Fig. 2J). Approximately 2000 DEGs were identified based on the filtering criteria (Fig. 2, H to J). In the IAN resection group, Gene Ontology (GO) annotation analysis indicated that these genes were highly enriched in known biological processes involved in the immune system and responses to stimuli (fig. S1B). Moreover, Kyoto Encyclopedia of Genes and Genomes (KEGG) enrichment analysis revealed that most DEGs were enriched in several immune-associated signaling pathways, including the Jak-STAT (*24*), NOD-like receptor (*25*), PI3K-Akt (*26*), and B cell receptor signaling pathways (Fig. 2K). These results highlighted the potent effects of IAN resection on the local immune microenvironment during bone regeneration. Neuropeptides and neurotransmitters released from sensory terminals functionally affect innate and adaptive immune cells, such as dendritic cells, neutrophils, mast cells, and macrophages, to regulate the immune response and inflammation in the vasculature and lymphatic vessels, host-pathogen defense, and inflammatory diseases (*21*). Considering that myeloid cells, such as macrophages, constitute most immune cells in injured bone tissues undergoing repair or regeneration (*27*), gene set enrichment analysis (GSEA) associated with macrophages was performed, which showed positive enrichment of related gene sets in the bone defect area, emphasizing the functional activation of macrophages in the early stage after sensory nerve dissociation (Fig. 2L).

This was further supported by histological analysis results (Fig. 2M). Immunohistochemical staining for calcitonin gene–related peptide (CGRP) and dopamine, which are specific markers for sensory and sympathetic nerves, respectively, indicated nerve ingrowth at the site of the bone defects. A large number of CGRP$^+$ cells were identified after 1 week in the sham group, and the count increased at week 2, suggesting that sensory nerves started to grow into the bone defect area in the early stages of bone regeneration, which is consistent with the findings of a previous study (*23*). However, almost no CGRP$^+$ sensory fibers remained after IAN transection throughout the inflammatory stage (Fig. 2, M to Q). The staining results for dopamine indicated stable expression over the experiment duration, with similar expression in both groups. Immunofluorescence staining in the defect area suggested the same trend. The numbers of CGRP$^+$TUBB3$^+$ (βIII-tubulin, a common marker of nerve fibers) sensory nerve fibers after IAN transection were significantly decreased at 1 week compared to the sham (14.01 ± 8.44 versus 44.88 ± 5.67%) and further declined at 2 weeks after surgery (fig. S2, A and B). However, the numbers of Dopamine$^+$TUBB3$^+$ sympathetic fibers remained unchanged after surgery in the two groups at both 1 and 2 weeks (fig. S2, A and B). These outcomes indicate that sensory nerves were removed from the bone defect area after IAN resection, but the number of sympathetic nerves was unaffected. Subsequently, as illustrated by H&E and Masson staining, substantially more infiltrated inflammatory cells were observed within the defect area of the denervation group at two time points compared with those in the sham group (Fig. 2M). These results were in agreement with the outcomes of transcriptome sequencing, which showed that inflammatory reactions occurred and were dysregulated after sensory denervation.

To further validate the important role of macrophages induced by IAN resection during inflammation, the macrophage functional phenotypes were investigated. Immunohistochemical analysis showed that inducible nitric oxide synthase–positive (iNOS$^+$) (a M1 marker) cells were predominant in the bone defect area in both groups at 1 week, demonstrating that the tissues exhibited M1 macrophage–mediated inflammatory responses (Fig. 2, M and R), which was consistent with the findings of previous reports (*28*, *29*). Two weeks after injury, the number of CD206$^+$ (a M2 marker) cells was greater than the iNOS$^+$ cells in the bone defect area in the sham group, suggesting a physiological transition from M1-mediated inflammation to M2-mediated repair (Fig. 2, M and S). However, after IAN resection, iNOS$^+$ cell infiltration persisted throughout the newly formed fibrous tissues at 2 weeks, along with decreased expression of CD206, indicating a strong inflammatory response (Fig. 2, M, R, and S). Similarly, immunofluorescence staining revealed that the number of iNOS$^+$CD68$^+$ and CD86$^+$CD68$^+$ M1 macrophages significantly increased after denervation, whereas the number of CD206$^+$CD68$^+$ and CD163$^+$CD68$^+$ M2 macrophages was inversely decreased at 1 and 2 weeks after surgery (fig. S3, A and B). Notably, after 4 weeks of denervation, the M1 percentage in the denervated group still remained a high level compared to the sham (fig. S3, C and D), indicating the delayed M1-dominant inflammation and impaired M1/M2 transition during bone regeneration without sensory innervation. In addition, flow cytometry analysis of macrophages and enzyme-linked immunosorbent assays (ELISAs) of tumor necrosis factor–α (TNF-α) and interleukin-10 (IL-10) provided further verifications of persistent and intense inflammatory responses induced by denervation (fig. S3, E to G).

Overall, these data demonstrated that the absence of sensory nerves resulted in the delayed polarization of macrophages toward an anti-inflammatory and pro-repair (M2-like) phenotype in the bone defect area. This, in turn, sustained the inflammatory stage, leading to impaired bone healing. Notably, these findings aligned with those of previous reports showing the anti-inflammatory effect and healing potential of sensory innervation by regulating the immune microenvironment in disease models such as diabetic foot and acute lung injury, as well as in other organs such as skin, joints, and gastrointestinal tract (*30*, *31*). Given that sensory denervation leads to greatly intensified and persistent inflammation in the bone defect area, we hypothesized that artificial promotion of sensory nerve ingrowth would produce the opposite effect and thus endogenously drive macrophage polarization from the M1 to M2 phenotype, subsequently facilitating the shift from the inflammatory stage to the repair stage during the early phase of bone repair. This led us to develop a platform that can specifically promote rapid sensory nerve ingrowth to achieve pro-healing immunomodulation for bone regeneration.

Sensory nerve–targeting peptides were screened by phage display

To the best of our knowledge, no molecules or drugs that specifically induce sensory nerve growth have been reported previously. To overcome this limitation, we constructed a bioactive molecule that facilitates sensory innervation. Specifically, we first screened sensory nerve–targeting molecules and then endowed the identified molecules with the capacity for sensory nerve induction.

As a novel biological manufacturing technology, bacteriophage displays have received increasing attention in the field of tissue engineering in recent years because of their low cost, high biocompatibility, and efficiency (*32*). Thus, we first screened sensory nerve–targeting peptides using the phage display technique (Fig. 3A). A library of M13 phage–displayed random 9-nucleotide oligomer peptides was

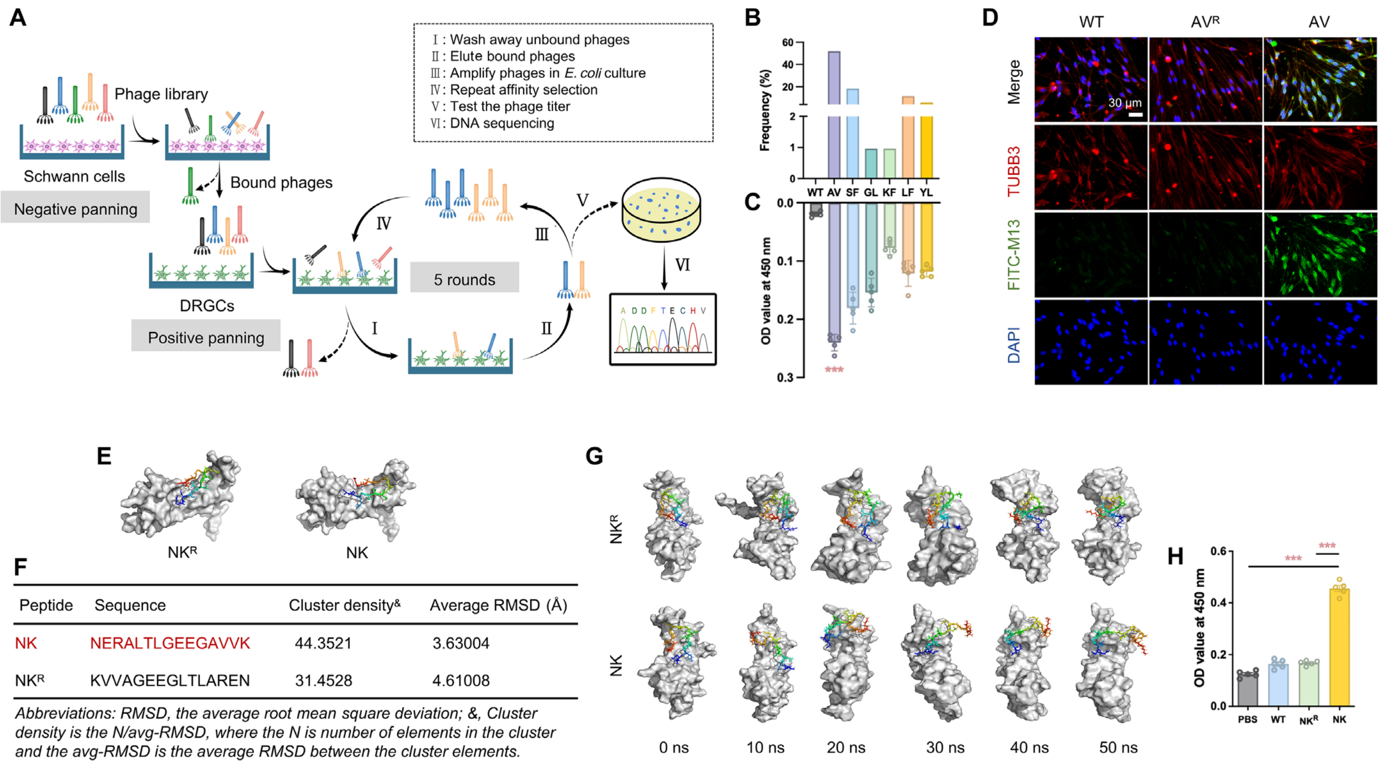

Peptide	Sequence	Cluster density&	Average RMSD (Å)
NK	NERALTLGEEGAVVK	44.3521	3.63004
NKᴿ	KVVAGEEGLTLAREN	31.4528	4.61008

Abbreviations: RMSD, the average root mean square deviation; &, Cluster density is the N/avg-RMSD, where the N is number of elements in the cluster and the avg-RMSD is the average RMSD between the cluster elements.

Fig. 3. Discovery of sensory neuron targeting peptides and functional verification of an NGF-binding peptide. (**A**) Schematic diagram of the screening of sensory neuron targeting peptides from a library of random M13 phage–displayed peptides. (**B**) Occurrence frequencies of selected sensory neuron–binding peptides after biopanning. (**C**) The phage ELISA demonstrated the binding between sensory neurons and the phages displayed peptides with a high occurrence frequency in biopanning. (**D**) Fluorescence staining to demonstrate the binding abilities of AV-displaying phages in vitro. The WT, AV-displaying, and AV^R (the reversed sequence of AV)–displaying M13 phages were labeled with FITC dyes and added to the medium containing sensory neurons (marked with TUBB3). Scale bar, 30 μm. (**E**) MD simulation of the binding between the β-NGF protein (gray) and the identified NK peptide (rainbow). CABS-docking modeling of NK and NK^R (reversed sequence of NK) peptides bound to β-NGF. (**F**) Density of the peptide clusters bound to the β-NGF protein. (**G**) MD simulation snapshots of β-NGF interacting with NK and NK^R visualized using Visual MD with a 10-ns interval and a total duration of 50 ns. (**H**) ELISA results of the interaction between β-NGF and the phage-displayed NK and NK^R peptides. ***$P < 0.001$.

used to interact with dorsal root ganglion cells (DRGCs) through biopanning. After an initial round of negative panning of Schwann cells, five rounds of positive panning toward DRGCs were then carried out, with titers of the eluted target-binding phages at 4.3×10^4, 3.4×10^5, and 3.7×10^5 plaque-forming units (PFU)/ml for rounds 3, 4, and 5, respectively (Fig. 3A). When the DRGC-binding phages were successfully enriched, the DNA of 104 phage plaques (53 and 51 in the fourth and fifth rounds, respectively) was randomly chosen for sequencing to determine the target-binding peptides displayed on the phages. As shown in Fig. 3B and table S1, one peptide, ADDFTECHV (termed AV), was predominant, with a total of 55 repeats, whereas the other screened peptides exhibited fewer repeats, suggesting that AV had been evolutionarily selected and potentially had the highest affinity for DRGCs. Therefore, AV-displaying phages were selected for further validation and investigation. A phage ELISA showed that AV-displaying phages had the highest affinity for DRGCs, with the maximum absorbance value (Fig. 3C), compared to wild-type (WT) phages and five other peptide-displaying phages (termed SF, GL, KF, LF, and YL, selected based on the sequence data in table S1). Moreover, to exclude any nonspecific binding of the peptide, immunofluorescence staining was conducted using the reversed sequence VHCETFDDA (termed AV^R) as the control. As shown in Fig. 3D, the DRGCs were clearly visualized by TUBB3 and only a substantially small portion of cells were stained by fluorescein isothiocyanate (FITC)–labeled WT or AV^R phages, demonstrating that there was no specific affinity between the DRGCs and these two types of phages. In contrast, a high FITC signal was detected after adding the AV phages for binding, and the quantitative results showed that the fluorescence intensity of FITC in the AV group was almost fourfold higher than that in the WT and AV^R groups (fig. S6). In addition, a similar investigation using PC-12 cells (a sympathetic nerve cell line, marked by Tyrosine Hydroxylase) as a replacement for DRGCs was performed to exclude the potential binding of AV phages toward sympathetic nerve (fig. S7). Expectedly, no FITC signal was detected in all three groups, indicating the lack of sympathetic affinity of the AV phages. Together, these data suggested that AV-displaying phages had a high binding affinity for DRGCs, which enabled the specific targeting of sensory neurons.

The affinity of β-NGF–binding peptide was successfully validated in vitro

The AV peptide had the ability to target sensory neurons; therefore, we attempted to endow the AV-displaying phages with the capacity to promote sensory innervation. It is well known that a variety of factors can influence sensory nerve regeneration, including glial cell line–derived neurotrophic factor (GDNF), fibroblast growth factor 2

(FGF-2), β-subunit of nerve growth factor (β-NGF), neurotrophin-3 (NT-3), brain-derived neurotrophic factor (BDNF), and transforming growth factor–β1 (TGF-β1) (*33–35*). Among these, β-NGF is particularly recognized for its essential role in the development, maintenance, and function of sensory neurons across various tissues (*36–38*). In the context of bone repair, β-NGF offers unique advantages: It is abundant in bone tissue and is derived from multiple sources, including Schwann cells, bone marrow stromal cells, osteoblasts, and osteoblastic cell lines (*39*). Besides, β-NGF is present at the earliest stage of bone injury, unlike other factors such as BDNF, which appear later (*2*). These characteristics make β-NGF an ideal target for promoting early-stage sensory innervation in local bone tissues. However, the abundant free NGF secreted within the inflammatory microenvironment cannot be specifically enriched around damaged sensory nerve fibers owing to the lack of chemotactic induction (*40*). To address this limitation, we initially considered chemically linking the AV neuropeptide directly to NGF to promote local sensory regeneration. However, because of the much larger molecular weight of NGF (~17 kDa for rat β-NGF) compared with that of the single peptide, it is unfeasible to either make phages directly express the related genes of NGF or to connect NGF onto the surface of phages (*41*). In addition, the sensitivity of NGF to inactivation and decomposition, as well as its high requirements for preservation and sterilization, limit its direct clinical application (*41*). Considering the abundance of NGF at the site of fractures in the early stage after injury (*13*), identifying a peptide with high NGF affinity to recruit autologous NGF that specifically targets sensory nerves to facilitate sensory innervation is a promising alternative therapeutic approach.

A previous study reported a high-affinity rat NGF-binding sequence, NERALTLGEEGAVVK (termed NK), which remarkably promoted neurite outgrowth in vitro with amphiphile nanofibers (*42*). In this study, to confirm the NGF-binding ability of NK peptide, we constructed a protein model of β-NGF (Fig. 3E) and predict the probable docking sites for NK and its reversed sequence (termed NK^R, selected for comparison) to bind β-NGF. The cluster density and the average root mean square deviation (avg-RMSD) of both NK and NK^R peptides were assessed (Fig. 3F), and the molecular dynamics (MD) simulation at a 10-ns interval indicated that the NK peptide had a more stable binding energy for β-NGF compared with that of NK^R as the latter exhibited instability from 30 ns (Fig. 3G). Moreover, phage ELISA was conducted on the NK peptide and its reversed sequence. As predicted, NK-displaying phages had the best affinity to β-NGF with a fourfold increase in absorbance, whereas WT and NK^R-displaying phages showed no significant difference in absorbance compared with that of the blank group (Fig. 3H). Collectively, both the MD simulation and ELISA results verified the high β-NGF–binding affinity of the NK peptide.

Double-displayed nanofibers were prepared and characterized

Subsequently, the M13 phages were genetically engineered to double display the two characterized peptides (AV, the sensory neuron–homing peptide, and NK, the β-NGF–binding peptide) (Fig. 4A). Specifically, the AV peptide was fused to the exposed terminal of the PIII region at one distal end of the M13 phages to obtain M13-AV phages. Then, the NK peptide was genetically fused to the exposed terminal of the PVIII region on the side surface of the M13-AV phages, and the resulting dual-functional phages were termed M13-AV-NK phages. DNA sequencing of the M13-AV-NK phages detected the base sequences of both AV and NK, confirming successful dual display at the desired sites (Fig. 4B). Similarly, nucleic acid electrophoresis showed a new band at ~500 base pairs (bp) corresponding to the engineered M13-AV-NK phages, whereas the WT phages lacked this band (Fig. 4C). For further comparison, AV^R and NK^R were displayed as alternative sequences for AV and NK, respectively, and a total of four types of phages were constructed: WT, M13-AV^R-NK, M13-AV-NK^R, and M13-AV-NK (abbreviated here as WT, AV^R-NK, AV-NK^R, and AV-NK, respectively). To confirm the binding affinity of these four phages for sensory neurons and β-NGF, corresponding ELISAs were performed. Although AV- NK^R and AV^R-NK only exhibited a small increase in absorbance, as expected, the absorbances of the AV-NK phage for both DRGCs and β-NGF were notably increased, revealing that both the AV and NK peptides were correctly fused to the phages and their functions (sensory nerve–targeting and β-NGF–binding, respectively) were conserved after being displayed (Fig. 4, D and E). Immunofluorescence staining of DRGCs and FITC-labeled phages further verified the ability of AV-NK to target sensory neurons. AV-NK^R and AV-NK, two phages displaying AV peptides on their PIII regions, displayed a significant increase in FITC signals, which were colocated with TUBB3 signaling from DRGCs. However, almost no M13 phages were specifically stained in the WT and AV^R-NK groups, suggesting their lack of affinity for sensory neurons due to the lack of the AV peptide (Fig. 4F). The fluorescence intensities of FITC in the AV-NK^R and AV-NK groups were similar, and they were more than four times that of the WT and AV^R -NK groups (fig. S8). Together, these results indicated that both AV and NK maintained their high affinity for DRGCs and β-NGF, respectively, after being displayed on the PIII and PVIII regions, respectively; therefore, the M13-AV-NK phages were used for subsequent treatment experiments.

Typically, uncontrolled chemical conjugation is indispensable for adhering peptides to nanoparticle surfaces to achieve their intended function (*43*). In this study, sensory neuron–targeting and NGF-binding peptides were site-specifically fused to coat proteins on the surface of nanofibers using a genetic engineering approach. Genetically engineered nanofibers are cheaper to produce than conventional chemically synthesized peptides or recombinantly expressed antibodies owing to their simple amplification and mass production using bacteria, which makes them promising for extensive production and application. Previous attempts to engineer innervated bone biomaterials mainly focused on the exogenous promotion of sensory nerve growth, relying on implanted nerve tracts or metal implants (*18*). However, autologous nerve grafts may damage donor areas and the ions released from metal implants may induce other potential side effects. These factors greatly limit the direct clinical application of the current strategies. In addition, direct administration of exogenous β-NGF may induce excessive sympathetic nerve ingrowth as overactivation of sympathetic nerves can hinder bone repair (*44*, *45*) and potentially trigger inflammatory responses (*46*), as well as pose potential side effects like skeletal pain (*47*). In the present study, these nanofibers enabled an approach for using autologous components to drive the ingrowth of impaired sensory nerves, with no obvious biological toxicity or other side effects.

M13-AV-NK phages specifically promote sensory nerve growth in vitro

Numerous studies have demonstrated the biocompatibility of phages (*48*, *49*). In this study, we further examined the biotoxicity of M13-

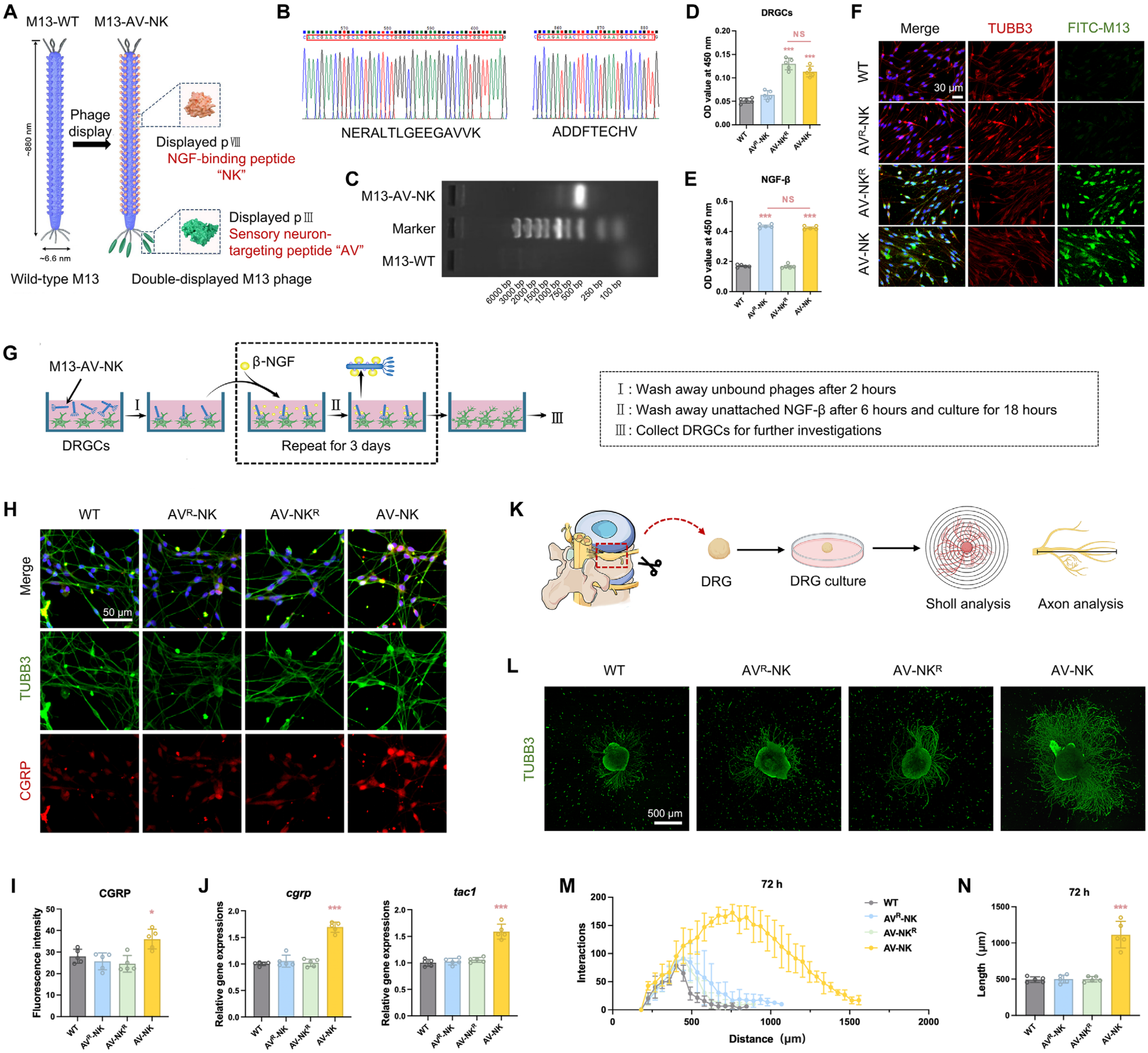

Fig. 4. Construction and functional verification of the dual-function phages. (**A**) Schematic representation of the doubled-displaying phages. The genetically engineered M13-AV-NK phages displayed sensory neuron–targeting (AV, fused to pIII at the tip) and NFG-binding peptides (NK, fused to pVIII on the side wall). (**B**) DNA sequencing of the dual-displaying phages to verify the successful insertion of the sequences encoding the AV and NK peptides. (**C**) Nucleic acid electrophoresis images of M13-WT and M13-AV-NK phages. (**D** and **E**) ELISAs showed the binding abilities of the M13-AV-NK phages for sensory neurons and β-NGF. (**F**) Fluorescence staining to determine the binding abilities of M13-AV-NK phages for sensory neurons (marked with TUBB3). Scale bar, 30 μm. (**G**) Schematic diagram of the sensory neuron culture model with periodic administration of exogenous β-NGF in vitro to simulate the in vivo microenvironment. β-NGF was added to the basic culture medium containing sensory neurons, which were pretreated with M13-AV-NK phages, and left for a short period of time before being removed by washing. The same process was conducted once a day for 3 days. (**H**) Immunofluorescence staining and (**I**) the corresponding quantification of TUBB3 and CGRP expression in sensory neurons. Scale bar, 50 μm. (**J**) Relative mRNA expression levels of *Cgrp* and *Tac1* in different groups at 72 hours. (**K**) Schematic representation of DRG explant culture in the same model as illustrated in (G) and evaluations, including Sholl analysis and axon analysis. (**L**) Immunofluorescence staining of TUBB3 to evaluate the axon growth of DRG explants in different groups after 72 hours of culturing. Scale bar, 500 μm. (**M**) Sholl plots and (**N**) axon tracing analysis results of M13-AV-NK–promoted neurite growth in in vitro DRG explants cultures with added β-NGF. h, hours. *$P < 0.05$; ***$P < 0.001$; NS, not significant.

AV-NK phage in DRGCs. Live/death staining showed that the application of phages (including WT and M13-AV-NK) had no effect on the viability of DRGCs as the level of cell death was low (red fluorescence) (fig. S9). Next, to verify the therapeutic effect of the dual-functional M13-AV-NK phages for sensory innervation in vitro, we mimicked the in vivo microenvironment by periodically adding exogenous β-NGF to in vitro cell cultures (Fig. 4G) to overcome the lack of endogenous β-NGF. Immunofluorescence staining of CGRP demonstrated a higher intensity of positive signals in DRGCs induced by M13-AV-NK with the addition of β-NGF, which was ~30% higher than the levels observed in the other three groups (Fig. 4, H and I). Similar to CGRP, substance P (SP) is a classical neuropeptide synthesized from preprotachykinin-A (TAC1) and is specifically associated with DRGCs (*50*). Thus, we measured the mRNA levels of CGRP and TAC1 using quantitative reverse transcription polymerase chain reaction (qRT-PCR). We found that the mRNA levels of CGRP and TAC1 were both up-regulated, particularly the expression of CGRP, which exhibited a nearly twofold increase (Fig. 4J), suggesting that DRGC growth was promoted by M13-AV-NK phages via β-NGF recruitment. However, the expression levels of both indicators were significantly lower in the WT, AV^R-NK, and $AV\text{-}NK^R$ groups (Fig. 4J), likely due to their lack of ability to bind DRGCs and β-NGF.

To better simulate in vivo sensory nerve innervation, explants of DRG were cultured in a similar manner of DRGC culturing mode (Fig. 4K). First, neurofilament staining of the explants was conducted, and the staining images showed that M13-AV-NK phages facilitated remarkable neurite extension in the DRG at 72 hours (Fig. 4L). Sholl analysis and axon tracing were used to assess neurite branching and axon length from the explant body. Compared to the other three groups, DRG explants treated with M13-AV-NK phages exhibited a significant increase in NGF-promoted branching and axonal growth (Fig. 4, M and N), indicating that the dual-displaying phages were capable of effectively promoting DRG growth in an NGF environment. Together, the above outcomes suggested that the dual-function M13-AV-NK phages were able to successfully bind the free β-NGF and specifically target sensory nerves to accelerate sensory innervation, thus having potential application in vivo.

A double-displayed phage-based bone repair system was constructed

On the basis of the observation that M13-AV-NK phages bind the free β-NGF that specifically targets DRGCs, we next explored whether local delivery of M13-AV-NK phages could specifically facilitate sensory innervation in vivo. However, the small size of phages poses a challenge for achieving sustained effects. Local application of large doses of phages might lead to immediate burst signaling as they can rapidly signal to cells, diffuse away from the delivery site, and be eliminated by the hepatobiliary and urinary organs of the reticuloendothelial system in a short period of time (*51*). Therefore, it is necessary to develop a composite system that enhances phage retention and enables sustained release of the phages to achieve long-term effects.

β-Tricalcium phosphate (β-TCP) is a bioceramic material that has been widely used in clinic as a bone substitute to improve osteoarticular injuries and diseases. Previous studies have shown that β-TCP has the ability to effectively load phages (*52*, *53*), due to strong interactions between carboxyl groups on phages and matrix-bound calcium (*54*), and gradually release them over while maintaining their biological activity (*55*). On the basis of these properties, β-TCP was selected in this study to allow for a more controlled and sustained release of phages. The average particle size of β-TCP is 2044 ± 543.5 nm, with polydispersity index (PdI) of 0.104 determined by dynamic light scattering (DLS; fig. S10). Transmission electron microscopy (TEM) showed that the dense nanofibrous phages were attached to β-TCP particles, indicating the potential capacity for β-TCP to load phages (Fig. 5C).

However, the disadvantages of β-TCP, such as brittleness, insufficient mechanical strength, and poor bone healing induction ability, hinder its direct application for bone repair (*56*). To address this, a hydrogel containing type I collagen, a natural component of bone, was used in this study to encapsulate phage-loaded β-TCP because of its good osteogenic potential, as well as its injectability, biodegradability, and biocompatibility (Fig. 5A) (*57*, *58*). Furthermore, collagen I (Col I) is also reported to support axonal growth and guidance in neural development and considered to be a good candidate for nerve tissue regeneration (*18*, *59*). Gelation of the hydrogels mediated by genipin was demonstrated by the change in color from semitransparent white to dark gray, suggesting the successful cross-linking (Fig. 5B). Consequently, a localized phage-based bone repair composite system (termed M13-AV-NK/β-TCP/Col I) was then constructed for further experiments (Fig. 5, A and B), with five experimental groups: (i) Col I: Col I hydrogel, (ii) g-Col I: genipin–cross-linked Col I hydrogel, (iii) β-TCP/g-Col I: β-TCP–incorporated genipin–cross-linked Col I hydrogel, (iv) WT/β-TCP/g-Col I: WT phage-loaded β-TCP–incorporated genipin–cross-linked Col I hydrogel, and (v) M13-AV-NK/β-TCP/g-Col I: M13-AV-NK phage-loaded β-TCP–incorporated genipin–cross-linked Col I hydrogel.

The releasing efficiency of phages from the M13-AV-NK/β-TCP/g-Col I hydrogels at different time points was first examined using plaque counting, the gold standard method for phage enumeration (Fig. 5D). The results showed that the titers of released phages gradually decreased with time, and few phage locus coerulei were observed on the plate at 28 days (Fig. 5, E and F). In addition, as the phages were able to efficiently lyse bacteria, an *Escherichia coli* lysis test was conducted to indirectly determine the phage titer by culturing the released phages with *E. coli* (Fig. 5D). These results further confirmed a long-term phage release as the number of colony-forming units continuously increased from days 1 to 28, suggesting a decreased number of infective phages for the lysis of *E. coli* (Fig. 5, G and H). However, after an initial burst release, only a limited number of phages were detected at 7 days released from the M13-AV-NK/g-Col I hydrogels without β-TCP, and almost no phage locus coerulei was observed at days 14 and 28 (fig. S11, A and B), indicating the essential role of β-TCP in controlling smooth release of phages. The corresponding results of agar plate cultivation of *E. coli* shared the same trend with only about a 7-day lysis efficiency (fig. S11C). In summary, these results demonstrated that phages were steadily released from the M13-AV-NK/β-TCP/g-Col I hydrogels over 28 days, offering a potential platform for long-lasting biological applications.

Moreover, attenuated total reflectance–Fourier transform infrared spectroscopy (ATR-FTIR) showed a characteristic peak at 1123 cm^{-1} in the Col I group, representing C—N stretching, which disappeared in the other four groups after genipin administration. These results further indicated the formation of amide covalent bonds within the hydrogels after gelation (Fig. 5I). On the other hand, the storage modulus (G') and loss modulus (G'') results suggested enhanced

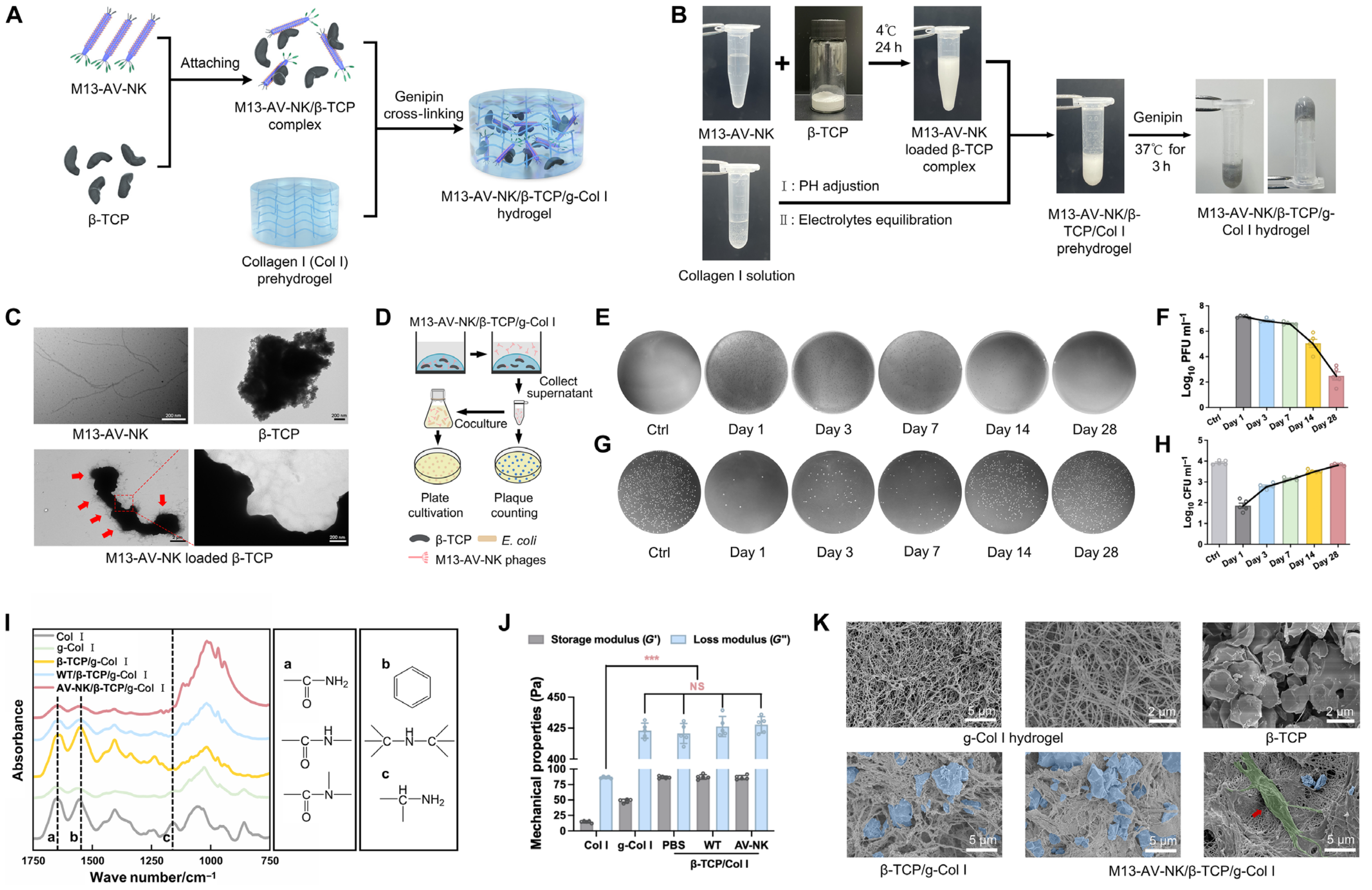

Fig. 5. Fabrication and characterization of the bone repair composite system. (**A**) Schematic diagram and (**B**) the specific construction processes of the M13-AV-NK/β-TCP/Col I composite hydrogel. (**C**) TEM images of M13-AV-NK, β-TCP, and M13-AV-NK–loaded β-TCP. The red arrows represent the M13 phages attached to β-TCP particles. Scale bars, 2 μm in the bottom left image and 200 nm for the other images. (**D**) Schematic diagram of the determination of phage release from the M13-AV-NK/β-TCP/Col I composite hydrogel. (**E**) Representative images of the phage locus coeruleus count and (**F**) the corresponding titer of the phages released from the M13-AV-NK–loaded β-TCP complex at different time points. (**G**) Representative images and (**H**) quantification of agar plate cultivation of *E. coli* treated with the released phages from various time points. (**I**) ATR-FTIR spectra of the four different groups. The dotted lines (a to c) represent specific absorption peaks related to genipin-mediated cross-linking. (**J**) Mechanical properties of the different hydrogels. (**K**) SEM images of the different groups. The red arrow in the lower-right image indicates DRGCs growing on the surface of the M13-AV-NK/β-TCP/Col I hydrogel. $***P < 0.001$; NS, not significant. h, hours.

mechanical properties, caused by genipin, as both G' and G'' substantially increased after cross-linking (Fig. 5J). Scanning electron microscopy (SEM) revealed irregular phage-loaded β-TCP particles homogeneously distributed within a fine nanofibrous structure of the collagen hydrogel in the M13-AV-NK/β-TCP/g-Col I complex (Fig. 5K). We also observed that DRGCs stretched on the hydrogel surface and exhibited normal physiological morphology, including elongated axons, potentially indicating that the bone repair composite system is a bioactive platform for cell growth (Fig. 5K). In addition, hydrogel biocompatibility tests via live/death staining of three-dimensional (3D) cultured DRGCs showed almost no red-stained dead cells in β-TCP/g-Col I hydrogels loaded with phages (fig. S12). Thus, the constructed M13-AV-NK/β-TCP/g-Col I complex had favorable biocompatibility.

The bone repair system specifically promotes sensory innervation and alleviates subsequent inflammation

First, a rat dorsal subcutaneous implantation model was conducted to evaluate the in vivo degradation rate of the composite hydrogel systems (fig. S13A). Both volume and mass of M13-AV-NK/β-TCP/g-Col I hydrogels declined steadily over time after implantation. At day 28, only 25.21 ± 8.45% of hydrogels were remained (fig. S13, B and C), indicating the acceptable degradability of the composited systems.

Next, to investigate the effect of sensory innervation specifically promoted by the dual-display phage-based system on bone healing, a rat mandibular critical-sized defect model was constructed to exclude the effects of spontaneous repair (Fig. 6, A to C). Three types of hydrogel complexes were injected into the defect area intraoperatively (Fig. 6, A and B): β-TCP/g-Col I, WT/β-TCP/g-Col I, and M13-AV-NK/β-TCP/g-Col I (abbreviated as Blank, WT, and M13-AV-NK, respectively).

Consistent with the in vitro results, the composite hydrogel systems showed similar releasing efficiency of phages. While the hydrogels presented red autofluorescence, the fluorescence intensity of the FITC-labeled M13 phages remaining in the hydrogel gradually decreased with time, and only sporadic fluorescence signal was detected after 28 days of implantation (fig. S14, A and B). In addition,

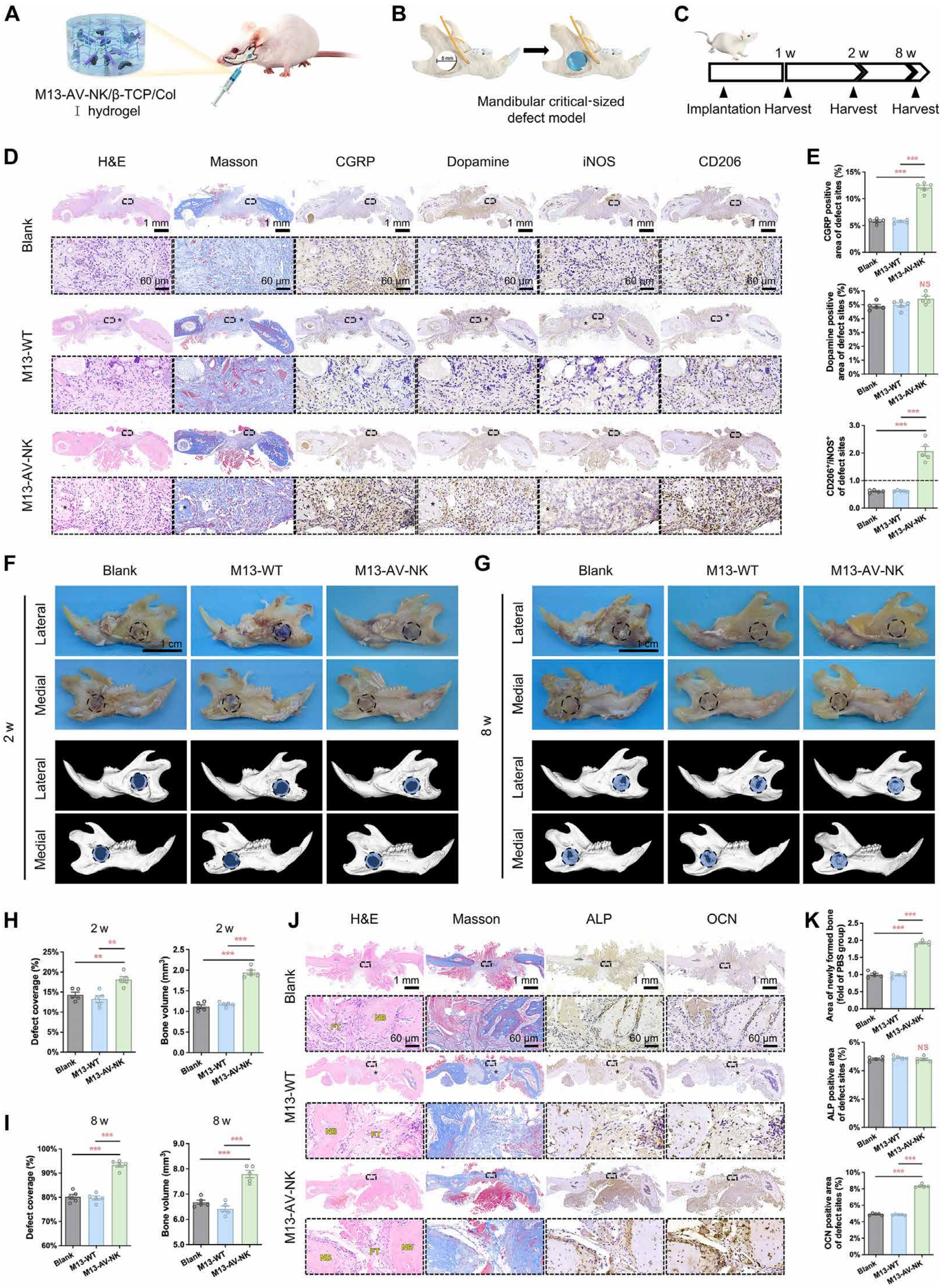

Fig. 6. Bone repair system promotes sensory innervation in vivo to inhibit the inflammatory response and improve bone healing. (**A** and **B**) Schematic representation of the rat mandibular critical-sized defect model and injection of the M13-AV-NK/β-TCP/Col I hydrogel. (**C**) Timelines of the animal experiments. (**D**) Panoramic and enlarged images and (**E**) the corresponding quantitative analysis of H&E, Masson, and immunohistochemical staining (CGRP, Dopamine, iNOS, and CD206) results at 1 week after implantation. The black asterisks represent residual hydrogels. Scale bars, 1 mm and 60 μm, respectively. (**F** and **G**) Micro-CT photographs of mandibular samples and the corresponding 3D reconstruction images at 2 and 8 weeks after implantation. The black dotted circles in mandible photographs and the blue circles in reconstructed images represent the initial defect areas (diameter = 5 mm). Scale bars, 1 cm. (**H** and **I**) Quantitative analysis of coverage percentage and new bone volume at the defect site for both time points. (**J**) Panoramic and enlarged images and (**K**) the corresponding quantification of H&E, Masson, and immunohistochemistry staining (ALP and OCN staining) at 8 weeks after implantation. β-TCP/g-Col I, WT/β-TCP/g-Col I, and M13-AV-NK/β-TCP/g-Col I (abbreviated as Blank, WT, and M13-AV-NK, respectively). The black asterisks represent residual hydrogels. "FT" and "NB" in H&E images indicate fiber tissue and new bone tissue, respectively. Scale bars, 1 mm and 60 μm, respectively. $^{**}P < 0.01$; $^{***}P < 0.001$; NS, not significant.

the in vivo binding affinity of M13-AV-NK phages released from the composite hydrogels toward β-NGF was further verified. Although almost no phage was observed in the M13-WT group, a large number of phages were successfully detected and colocated with β-NGF (fig. S15), indicating the excellent binding capacity of M13-AV-NK–based composite hydrogels for β-NGF.

Local nerve innervation primarily occurs in the early stages of bone regeneration, particularly during the first 2 weeks (*23*). Thus, in this study, the ingrowth of sensory and sympathetic nerves was assessed using immunohistochemical staining of representative markers (CGRP and dopamine, respectively) 1 week after implantation (Fig. 6, C and D). A larger number of $CGRP^+$ nerve fibers were identified in the M13-AV-NK–treated area around the hydrogel compared with that in the Blank and WT groups in both immunohistochemistry and immunofluorescence analysis (Fig. 6, D and E, and fig. S16, A and B), suggesting that the continuous release of M13-AV-NK phages from the hydrogel complex promoted sensory nerve growth in the bone defect area. However, there was no substantial difference in the number of $Dopamine^+$ sympathetic fibers among the three groups (Fig. 6, D and E, and fig. S16, A and B), indicating that M13-AV-NK phages did not affect sympathetic nerve growth. Together, these results suggested that released M13-AV-NK phages could specifically accelerate sensory innervation in the early stage after injury in vivo.

As the dominant type of immune cells involved in inflammation, macrophages are crucial for inflammatory promotion and resolution, as well as in tissue restoration (*60*). Given that the above results demonstrated sensory innervation–macrophage interactions (Fig. 2, I to S), we assessed the expression of specific markers of macrophages to determine the changes in inflammation caused by M13-AV-NK-mediated sensory innervation. As shown in Fig. 6 (D and E) and fig. S17 (A and B), the M13-AV-NK group presented significantly increased infiltration of M2 macrophages ($CD206^+CD68^+$ and $CD163^+CD68^+$) and a much higher M2/M1 ratio than the Blank and WT groups, which was also verified by flow cytometry analysis (fig. S17C). In addition, the decreased TNF-α concentration and growing IL-10 concentration further suggested a favorable anti-inflammatory microenvironment induced by M13-AV-NK–based hydrogels (fig. S17D).

This revealed that the accelerated growth of sensory nerves induced macrophage transition from M1 to M2, which is usually regarded as a symbol of decreased inflammatory responses and transition to the bone repair stage (*14*). In summary, these results confirmed that the specific promotion of sensory nerves induced by the M13-AV-NK/β-TCP/g-Col I system prevented excessive inflammation and facilitated a faster transition toward the bone repair phase in the early stage after injury.

As reported, excessive and prolonged inflammatory responses under some pathological conditions result in microenvironmental dysregulation and subsequent disruption of healing processes (*19*). Various drugs (*61*), metallic materials (*62*), and hydrogels (*58*) have been developed and used to treat inflammation and bone regeneration. Herein, we creatively fabricated a double-displayed phage-based hydrogel system focusing on effective promotion of sensory innervation to induce the functional transformation of macrophage for attenuated inflammation after bone injury.

The bone repair system improves the outcome of bone healing

Considering that rapid sensory innervation and inflammation dispersion was induced by M13-AV-NK/β-TCP/g-Col I compound system, we further validated whether these physiological changes resulted in improved bone healing. Mandibular specimens were harvested 2 and 8 weeks after implantation, and the promoting effect of sensory innervation on repair in vivo was evaluated using micro-CT and histological analysis (Fig. 6, F to K). Although only a small amount of bone tissue was formed in the Blank and WT groups, owing to the limited inherent osteogenic potential of Col I hydrogels at 2 weeks postsurgery, the mandibular defects in the M13-AV-NK group were partially repaired with new bone tissue (Fig. 6, F and G). The osteogenic effect at 8 weeks in the M13-AV-NK group was significantly pronounced compared with that in the other two groups as the defects of the former were almost completely filled with new bone tissue (Fig. 6, F and G). The quantitative micro-CT results further validated these observations. After 2 weeks of implantation, the defect coverage percentage of the M13-AV-NK group was 18.12 ± 1.67%, which was higher than that in the Blank and WT groups (14.31 ± 1.47 and 13.29 ± 1.88%, respectively) (Fig. 6H). Furthermore, the bone volume was $1.95 \pm 0.13\ mm^3$ in the M13-AV-NK group, which was significantly larger than that in the other two groups (1.11 ± 0.10 and $1.18 \pm 0.05\ mm^3$, respectively) (Fig. 6H). The defect coverage percentage and new bone volume at 8 weeks after surgery exhibited the same trends as those at the previous time point (Fig. 6I). Both indices were highest in the M13-AV-NK group, in which sensory innervation was induced (93.42 ± 1.99% for the defect coverage and $7.79 \pm 0.32\ mm^3$ for the bone volume) (Fig. 6I). Collectively, these results indicated the remarkable benefits of the hydrogel composite system for bone healing.

H&E and Masson staining histological analyses at 8 weeks postimplantation showed that the volume of regenerated bone tissue was larger and the area of fibrous tissue surrounding the newly formed bone was remarkably smaller in the M13-AV-NK group compared with those in the Blank and WT groups (Fig. 6J). In addition, as shown in the immunohistochemical results, the brown-stained area of OCN^+ cells was larger in the M13-AV-NK group compared with those in the other two groups (Fig. 6J), further indicating the enhanced bone healing in the M13-AV-NK group. Notably, the areas of ALP^+ cells at 8 weeks after implantation were not significantly different between the three groups (Fig. 6, J and K), which might be because ALP is mainly expressed in the early stages of osteogenesis. To assess the osteoclast activity and angiogenic effects of different composite hydrogels, TRAP staining and immunofluorescence staining of CD31 were then performed, respectively. Although no remarkable change was observed in $TRAP^+$ cell numbers among the three groups (fig. S18A), CD31 was highly expressed in the M13-AV-NK group, suggesting positive effects of the anti-inflammatory microenvironment on vascularization during bone repairing (fig. S18B). Together, these results further supported the idea that the sensory innervation induced by the dual-displaying phage-based hydrogel after injury promoted the endogenous repair ability of bone tissue. In addition, no obvious pathological changes were observed in the heart, liver, spleen, lung, or kidney, suggesting that the composite hydrogels had excellent biocompatibility in vivo (fig. S19). Although existing neuralized materials mainly advocate the direct promotion of regenerative stage after bone injury, we highlighted the immunoregulation mediated by induction of sensory nerve growth occurs in the early stage of the healing process and verified the indirect bone repair effect facilitated by neuroimmune regulation.

IAN transection leads to therapeutic failure of the bone repair system

To validate whether anti-inflammatory immunomodulation and the bone pro-healing effects of the M13-AV-NK/β-TCP/g-Col I system were dependent on sensory innervation, we further resected the IAN from the rat mandibular critical-sized defect models for further investigations (Fig. 7A). The rats with or without denervated IANs (termed the denervation or sham groups, respectively) were all implanted with M13-AV-NK/β-TCP/g-Col I, euthanized at 1 week after surgery for histological evaluation of the early stage and evaluated at week 2 or 8 postimplantation to assess osteogenic effects (Fig. 7B).

H&E and Masson staining demonstrated that residual hydrogel was present in the defect areas after 1 week of implantation (Fig. 7C).

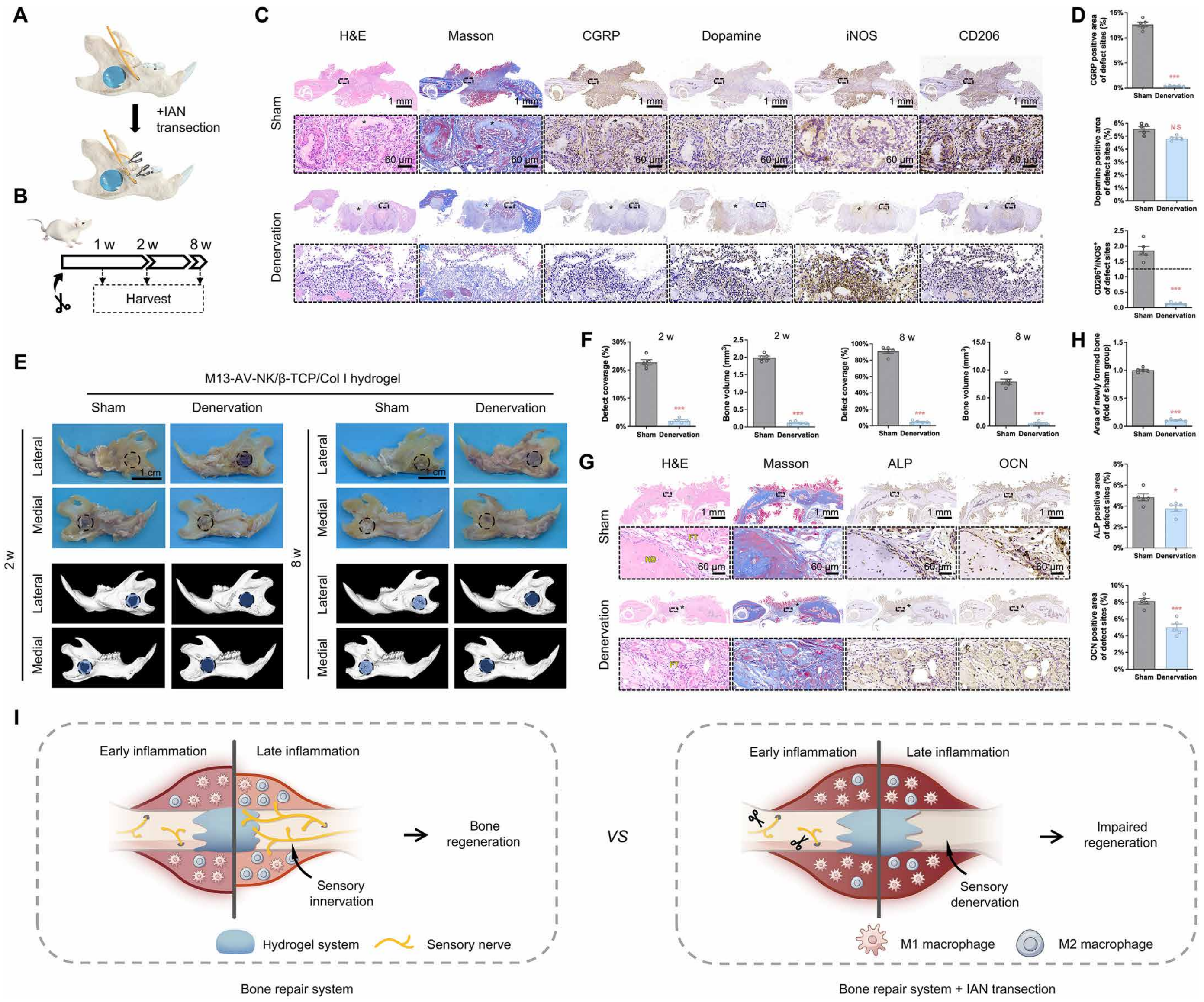

Fig. 7. IAN denervation leads to therapeutic failure of the bone repair system. (**A**) Schematic diagram of the rat mandibular critical-sized defect model with IAN denervation. Before M13-AV-NK/β-TCP/Col I hydrogel administration, the IAN was transected from rats in the denervation group, and a sham operation was conducted for the control group. (**B**) Timelines of the animal experiments. (**C**) Panoramic and partially enlarged images and (**D**) the corresponding quantitative results of H&E, Masson, and immunohistochemistry staining (CGRP, Dopamine, iNOS, and CD206) after 1 week of implantation. The black asterisks represent residual hydrogels. Scale bars, 1 mm and 60 μm, respectively. (**E**) Photographs of mandibular samples and the corresponding 3D reconstruction micro-CT images at 2 and 8 weeks after implantation. The black dotted circles in mandible photographs and the blue circles in reconstructed images represent the initial defect areas (diameter = 5 mm). Scale bars, 1 cm. (**F**) Quantitative analysis of 3D reconstruction results, including coverage percentage and the new bone volume of the defect region, of the two groups at different time points. (**G**) Panoramic and partially enlarged images and (**H**) the corresponding quantification results of H&E, Masson, and immunohistochemistry staining (ALP and OCN) after 8 weeks of implantation. The black asterisks represent residual hydrogels. "FT" and "NB" in the H&E images indicate fiber tissue and new bone tissue, respectively. Scale bars, 1 mm and 60 μm. (**I**) Schematic diagram of early-stage and late-stage inflammatory processes during bone healing in models administered the phage-loaded bone repair system with or without IAN transection. *$P < 0.05$; ***$P < 0.001$; NS, not significant.

Immunohistochemical and immunofluorescence images showed a significant increase in the expression of sensory nerve–specific marker CGRP in the local microenvironment in the first week (Fig. 7, C and D, and fig. S20, A and B), accompanied by increased numbers of $CD206^+CD163^+$ M2 macrophages in the nondenervated group (Fig. 7, C and D, and fig. S21, A and B). This indicated early rapid sensory neuralization after M13-AV-NK application in vivo and a shift of macrophages from the M1 to the M2 subtype, which contributes to reducing inflammation. These results were consistent with our aforementioned results. However, after sensory denervation through IAN resection, almost no $CGRP^+$ nerve fiber was found (Fig. 7, C and D, and fig. S20, A and B), suggesting that M13-AV-NK/β-TCP/g-Col I failed to promote sensory innervation in the context of complete sensory nerve removal. Moreover, dense $iNOS^+CD86^+$ M1 macrophage infiltration was detected in the visualized field of the denervation group, whereas low CD206 and CD163 expression was observed around the hydrogel (Fig. 7, C and D, and fig. S21, A and B). Flow cytometry analysis of callus also showed an extremely skewed M2/M1 ratio after 1 week of denervation (fig. S21C), combined with the abundant TNF-α and scarce IL-10 determined by ELISAs (fig. S21D), indicating a severe inflammatory response resulting from sensory denervation. Collectively, these results suggested that the promotive effects on sensory innervation and the inflammation reduction effects of the M13-AV-NK/β-TCP/g-Col I system were highly dependent on the extant sensory nerves.

Next, we explored whether the impairment of sensory innervation and persistence of inflammation after IAN resection would damage the induced osteogenesis effect in the early (2 weeks) and late (8 weeks) stages of injury. The micro-CT images and the corresponding gross specimens revealed that newly formed bone tissues effectively filled the defect areas in the sham group but were substantially blocked by IAN innervation at both 2 and 8 weeks (Fig. 7E). The defect coverage percentage of the sham group increased from 22.78 ± 2.11% at 2 weeks to 90.69 ± 5.60% at 8 weeks, and that of the denervation group significantly decreased from 2.00 ± 0.82 to 4.69 ± 1.59% at 2 and 8 weeks, respectively (Fig. 7F). Quantitative analysis of new bone volumes showed the same trend, with 1.99 ± 0.11 mm^3 versus 0.12 ± 0.04 mm^3 at 2 weeks and 7.92 ± 1.06 mm^3 versus 0.47 ± 0.29 mm^3 at 8 weeks postsurgery for the sham and denervation groups, respectively (Fig. 7F). Similarly, according to the H&E and Masson staining, the area of newly formed bone tissue in the sham group was approximately nine times that in the denervation group (Fig. 7G). Immunohistochemical staining images showed that the areas of ALP^+ and OCN^+ cells were larger in the sham group compared with those in the denervation group (Fig. 7, G and H). In addition, although no significant change of $TRAP^+$ cell numbers was observed between the two groups (fig. S22A), the expression of CD31 after denervation was rather remarkably reduced more than five times compared to that in the sham (fig. S22B). Together, these results highlighted the indispensable role of sensory innervation in bone repair promoted by M13-AV-NK/β-TCP/g-Col I, indicating that severe damage of sensory nerves would result in persistent inflammation, impaired revascularization and an unfavorable bone healing outcome (Fig. 7I).

The skeletal system has extensive sensory innervation, which enables the detection of changes in bone density and metabolic activity to maintain bone homeostasis (*18*). In addition, sensory nerves can control adaptation of the skeleton to mechanical loads, probably through NGF–tyrosine kinase receptor 1 (TrkA) signaling (*1*, *63*). Specific deletion of sensory nerves impairs bone mass accrual, and its malfunction or loss often leads to increased susceptibility to bone fracture and diminished bone regeneration after injury in patients (*6*). Although our phage-based hydrogel was capable of promoting sensory innervation in the early stages after injury to mediate inflammation alleviation and facilitate bone healing, its regenerative effect was dependent on a certain degree of residual functional sensory nerves. Thus, complete loss of local innervated sensory nerves following IAN resection reversed the therapeutic effect of the composite hydrogel, indicating that the hydrogel works primarily through sensory nerves rather than other components, which emphasizes the urgent need for the rescue of nerve function after injury (Fig. 7I).

Sema3A is involved in the sensory nerve–mediated macrophage polarization

Macrophages are the predominant immune cells involved in inflammation during the early stage after bone injury (*27*). They actively promote and resolve local inflammation and subsequent tissue restoration, usually through their phenotypic transition from the M1 to M2 subtype (*64*). Various pathogenic conditions cause delayed M1/M2 polarization, which leads to aggravation of inflammatory responses and impaired tissue regeneration (*13*). On the basis of our previous results indicating a negative change in the M1/M2 ratio induced by sensory denervation (Fig. 2), we explored whether sensory nerves could regulate the temporal transition of macrophages to drive repair processes in the early stages of bone regeneration.

To determine whether sensory nerves influence macrophage polarization in a paracrine manner, we cultured bone marrow–derived macrophages (BMDMs) in sensory neuron–derived conditioned medium (CM), a mixture of basal culture medium and the supernatant from the DRGC culture medium (Fig. 8A). Immunofluorescence staining and corresponding quantitative analysis showed that BMDMs highly expressed CD206 (an M2 marker), with an almost fourfold increase in fluorescence intensity after CM stimulation (Fig. 8, B and C). Moreover, the expression of the M2-secreted cytokine IL-10 was up-regulated after CM administration. However, the ELISA showed that the expression of TNF-α and IL-1β (both secreted by M1 macrophages) were not significantly different between the two groups (Fig. 8D). These findings suggested that sensory neurons might promote M2 polarization via the paracrine pathway.

As CGRP and SP are the most common neuropeptides secreted by sensory nerves (*12*), Chen and co-workers reported that CGRP application in vitro successfully induced murine macrophage M2 polarization in an acute lung injury model (*65*), and Xu and co-workers found that SP was closely related to the macrophage phenotype transition in alveolar lavage fluid in pediatric asthma (*66*). Thus, we investigated whether CGRP and SP in the CM were key factors in regulating macrophage polarization in the skeletal system by specifically inhibiting the function of CGRP or SP in the CM using specific neutralizing antibodies. Unexpectedly, immunofluorescence images and corresponding quantification results demonstrated that only the CGRP-neutralizing antibody was found to mildly inhibit M2 macrophage polarization, with a limited decrease in the red fluorescence of CD206 (fig. S23, A and B). Furthermore, the ELISA results for the relevant cytokines also showed that blocking both CGRP and SP had no obvious effect on macrophage polarization (fig. S23C). To figure out why the effect of CGRP was inconsistent with the findings of other in vitro studies, we measured the concentration of CGRP in the CM after 3 days of culture. The

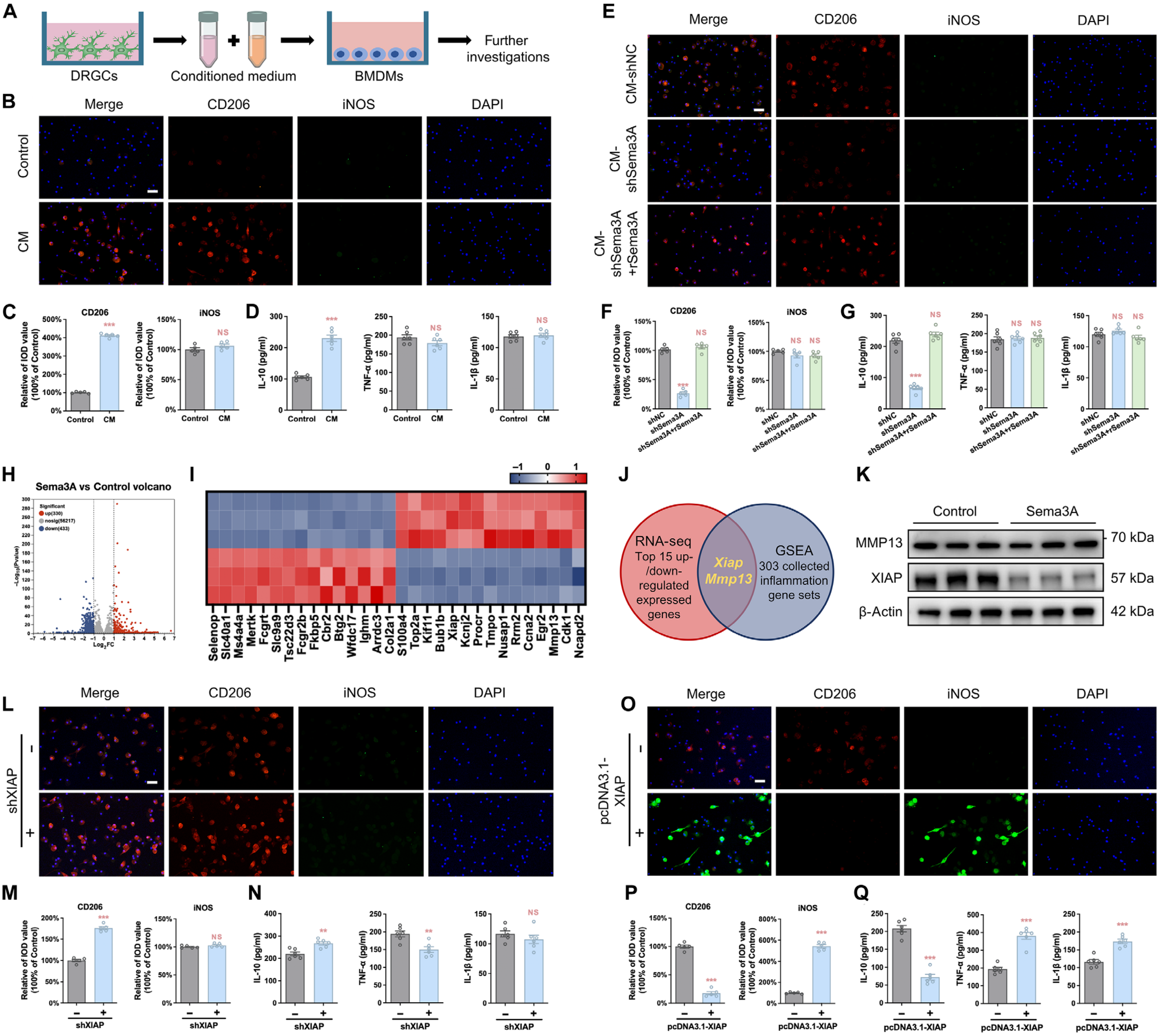

Fig. 8. Sema3A mediates XIAP expression to promote the M2 polarization of macrophages. (**A**) Schematic representation of macrophage conditioned culture. The supernatant of DRGC culture medium was collected and mixed with the conventional culture medium of macrophages in equal proportion to obtain the CM. (**B**) Immunofluorescence staining and (**C**) quantification of CD206 (M2 marker) and iNOS (M1 marker) expression in macrophages. Scale bar, 30 μm. (**D**) ELISAs of anti-inflammatory cytokine IL-10 and pro-inflammatory cytokines TNF-α and IL-1β. (**E**) Immunofluorescence staining and (**F**) the corresponding quantification of CD206 and iNOS expression in macrophages treated with CM from Sema3A-specific knockdown DRGCs and rSema3A. Scale bars, 30 μm. (**G**) ELISAs of IL-10, TNF-α, and IL-1β expression after culturing with different CMs. (**H**) Volcano plot of the differential gene expression in macrophages after Sema3A transfection. (**I**) Heatmap of the mRNA transcription profiles of the top 15 up-/down-regulated genes. (**J**) Venn diagram indicating the number of genes overlapping with those collected from the GSEA database (inflammation-related gene sets containing 303 different genes) and the top 15 up-/down-regulated genes screened using RNA-seq. Two genes (Xiap and Mmp13) were overlapping. (**K**) Representative Western blotting images of XIAP and MMP13 in macrophages after culturing with Sema3A. (**L** and **M**) Immunofluorescence images and the corresponding fluorescence intensity of CD206 and iNOS expression in macrophages after shXIAP transfection. Scale bar, 30 μm. (**N**) ELISAs of IL-10, TNF-α, and IL-1β after shXIAP transfection. (**O** and **P**) Immunofluorescence images and the corresponding quantitative analysis of CD206 and iNOS in XIAP-overexpressing macrophages transfected with pcDNA3.1-XIAP. Scale bar, 30 μm. (**Q**) ELISAs of IL-10, TNF-α, and IL-1β in macrophages overexpressing XIAP. IAN, inferior alveolar nerve; rSema3A, recombinant Sema3A. **$P < 0.01$; ***$P < 0.001$; NS, not significant.

concentration of CGRP secreted by DRGCs reached 7.87 ± 0.67 pM (fig. S23D), which was similar to that reported in the blood (*67*) and palatal epithelium (*68*) in vivo but was much lower than that required for the in vitro induction of macrophages (*69*). Collectively, these results indicated that there were other active factors in the CM that participate in macrophage polarization, instead of the neuropeptides at low physiological concentrations.

To screen the potential factors responsible for manipulating macrophage polarization, transcriptome sequencing was then performed. The DRGCs were treated with M13-AV-NK and M13-WT phages (as the control) using the same method as described in Fig. 4G. Exogenous β-NGF was periodically added into the cell culture medium to mimic the in vivo microenvironment. Among all the enriched signaling pathways listed in KEGG enrichment analysis, a nerve-related pathway (axon guidance) was specifically identified (fig. S24A). Further analysis of neuron-associated DEGs screened out two genes, including *Sema3A* and *Semaphorin 6A* (*Sema6A*), which are both axon guidance factors, and only the expression of *Sema3A* was up-regulated in the M13-AV-NK group (fig. S24B). These results led us to speculate that Sema3A might play a key role in CM-induced macrophage polarization. Previous researches have clarified that, in addition to common neuropeptides like SP and CGRP, sensory nerves communicate with tissues via locally released neurotransmitters, axon guidance factors, and neurotrophins (*39*). These molecules collectively participate in tissue metabolism and the maintenance of homeostasis (*21*, *70*). Sema3A, as a member of semaphorin family, was reported closely associated with immune regulation in various tissues (*71*). For instance, Sema3A effectively reduces the inflammatory response and improves cell physiological functions in lung (*72*) and cardiac tissues (*73*). However, its regulatory effects on macrophages in skeletal tissues remain unclear.

On the basis of the above results, we next explored the expression change of Sema3A following M13-AV-NK treatment. Both the mRNA level and protein expression level were significantly up-regulated after application of M13-AV-NK phages, as shown in fig. S24 (C to E). Similarly, immunofluorescence staining of TUBB3 and Sema3A showed that the fluorescence intensity of Sema3A in M13-AV-NK–treated DRGCs increased by nearly two times compared to the control (fig. S24, F and G), suggesting that M13-AV-NK phages were able to up-regulate the expression of Sema3A in sensory neurons through binding exogenous β-NGF. To figure out whether the in vivo expression of Sema3A was elevated with M13-AV-NK/β-TCP/Col I hydrogel administration, an immunofluorescence staining of Sema3A was then performed after 1 week of implantation. Consistent with in vitro investigations, Sema3A$^+$ area in the defect region was remarkably increased in the M13-AV-NK group (fig. S24, H and I). In addition, sparse Sema3A expression was observed in the M13-WT group, which we speculate originates from osteoblasts, osteocytes, and other resident cells (*74*, *75*). Together, these results indicated that M13-AV-NK phages might boost the Sema3A expression in the microenvironment by binding β-NGF to sensory nerves, the ingrowth of which has been previously verified to manipulate macrophage polarization. Consequently, this prompted us to further explore the influence of Sema3A on macrophages by specifically knocking down Sema3A.

As shown in Fig. 8E, almost no red fluorescence of CD206 was observed after culturing in CM from shSema3A-treated DRGCs, indicating inhibition of macrophage M2 polarization caused by Sema3A knockdown (Fig. 8E and fig. S25); however, this was reversed by subsequent treatment with recombinant Sema3A (Fig. 8E). The corresponding quantification (Fig. 8F) and ELISA results (Fig. 8G) also verified this finding. Although the expression of CD206 and IL-10 was significantly decreased after Sema3A knockdown, the expression of iNOS, TNF-α, and IL-1β remained unchanged under all conditions (Fig. 8, F and G). These results verified that Sema3A was the key bioactive factor mediating sensory nerve–induced M2 polarization.

XIAP participates in macrophage polarization mediated by Sema3A

To further understand the molecular mechanisms by which Sema3A modulates macrophages, we analyzed the transcriptomes of macrophages following Sema3A stimulation using RNA sequencing (RNA-seq). After ensuring the intergroup stability of the cell samples (fig. S26A), DEGs were analyzed. A volcano plot was generated, which indicated a pronounced change in the transcripts of macrophages cultured with Sema3A compared to those of the control (Fig. 8H). Furthermore, KEGG enrichment analysis showed that the IL-17 and TGF-β signaling pathways were enriched, which are closely associated with macrophage polarization (fig. S26B). To identify the key genes involved in macrophage polarization after Sema3A stimulation, the top 15 up-regulated and down-regulated DEGs were identified (Fig. 8I) and compared with genes in the inflammation gene sets from the GSEA database. Two overlapping genes, X chromosome–linked inhibitor of apoptosis protein (*XIAP*) and matrix metalloproteinase (*MMP13*), were identified (Fig. 8J). The expression levels of these two proteins were measured in Sema3A-induced macrophages. The results showed that XIAP expression was remarkably decreased compared to that in the control, whereas no obvious change in MMP13 expression was observed after culturing with Sema3A (Fig. 8K). Considering that both the transcription and protein levels of XIAP were significantly down-regulated after Sema3A induction (Fig. 8, I to K), we hypothesized that XIAP plays a crucial negative regulatory role in Sema3A-mediated macrophage polarization.

XIAP protein consists of three signature baculovirus IAP repeat (BIR) domains regulating protein-protein interactions and a Really Interesting New Gene (Ring) domain conferring E3 ubiquitin ligase activity (*76*). A previous study reported XIAP as an antiapoptotic factor with ubiquitination substrates for apoptotic caspases and Smac (*76*). Recently, researchers have found that XIAP participates in the regulation of inflammation in several tissues. For example, XIAP ubiquitinates RIPK2 to regulate the RIPK2-TAB1 inflammatory pathway and promote neutrophil infiltration in melanoma tissues (*77*). In addition, inhibiting the ubiquitination process of XIAP by RIP2 was found to block the NOD2 signaling pathway, resulting in inhibition of the development of inflammatory bowel disease and sarcoidosis (*78*). On the basis of these previous findings, we explored whether XIAP could mediate immunoregulation, especially macrophage polarization, in the skeletal system.

As expected, macrophages were polarized to the M2 phenotype after specific knockdown of XIAP through transfection of shXIAP (fig. S27A), with significantly increased CD206-related fluorescence (Fig. 8, L and M), up-regulated expression of IL-10, and down-regulated expression of TNF-α (Fig. 8N). However, overexpression of XIAP mediated by pcDNA3.1-XIAP (fig. S27B) induced increased macrophage polarization toward the M1 phenotype, as demonstrated by enhanced green fluorescence signals of iNOS expression (approximately fivefold that of the control; Fig. 8, O and P) and M1-related cytokine expression (TNF-α and IL-1β; Fig. 8Q). In addition, overexpression of XIAP resulted in a decrease of the concentration of IL-10 in the supernatant by more than 60% compared with that in the control (Fig. 8Q), indicating the inhibition of M2 polarization by XIAP. Together, these results indicated that Sema3A promoted M2 polarization, likely via the down-regulation of XIAP expression.

XIAP mediates PAX6 ubiquitination in macrophage polarization

Because of the ubiquitin ligase (E3) activity of XIAP, we investigated the potential interaction substrate of XIAP during the regulation of macrophage phenotype transition. A tandem mass tag (TMT)–based quantitative proteomic analysis was conducted to identify the differentially expressed proteins after XIAP knockdown using shXIAP (fig. S28), and the top five proteins with up-regulated and down-regulated expression were listed in a heatmap (Fig. 9A). In addition to the probable ubiquitination substrates of XIAP predicted using the UbiBrowser database, we screened Paired-box 6 (PAX6) as a potential binding partner of XIAP (Fig. 9B). PAX6 is a transcription factor that belongs to the highly conserved PAX family. This protein functions as a potent cell fate determinant in various processes, including the development of the central nervous system (*79*). Dysregulation of PAX6 activity is associated with developmental disorders and tumor formation (*79*). A previous study has identified the degradation of PAX6 by ubiquitination with the E3 ubiquitin ligase MID1 during vision development (*80*). However, whether XIAP can ubiquitinate PAX6 remains unknown.

To determine the potential interaction between XIAP and PAX6, Western blotting was performed, which confirmed that the expression level of PAX6 was negatively correlated with that of XIAP as its signal increased after XIAP knockdown (Fig. 9C). Moreover, after cotransfection of Myc-tagged XIAP and Flag-tagged PAX6 (abbreviated as Myc-XIAP and Flag-PAX6, respectively) plasmids in human embryonic kidney (HEK) 293T cell lines, coimmunoprecipitation (Co-IP)

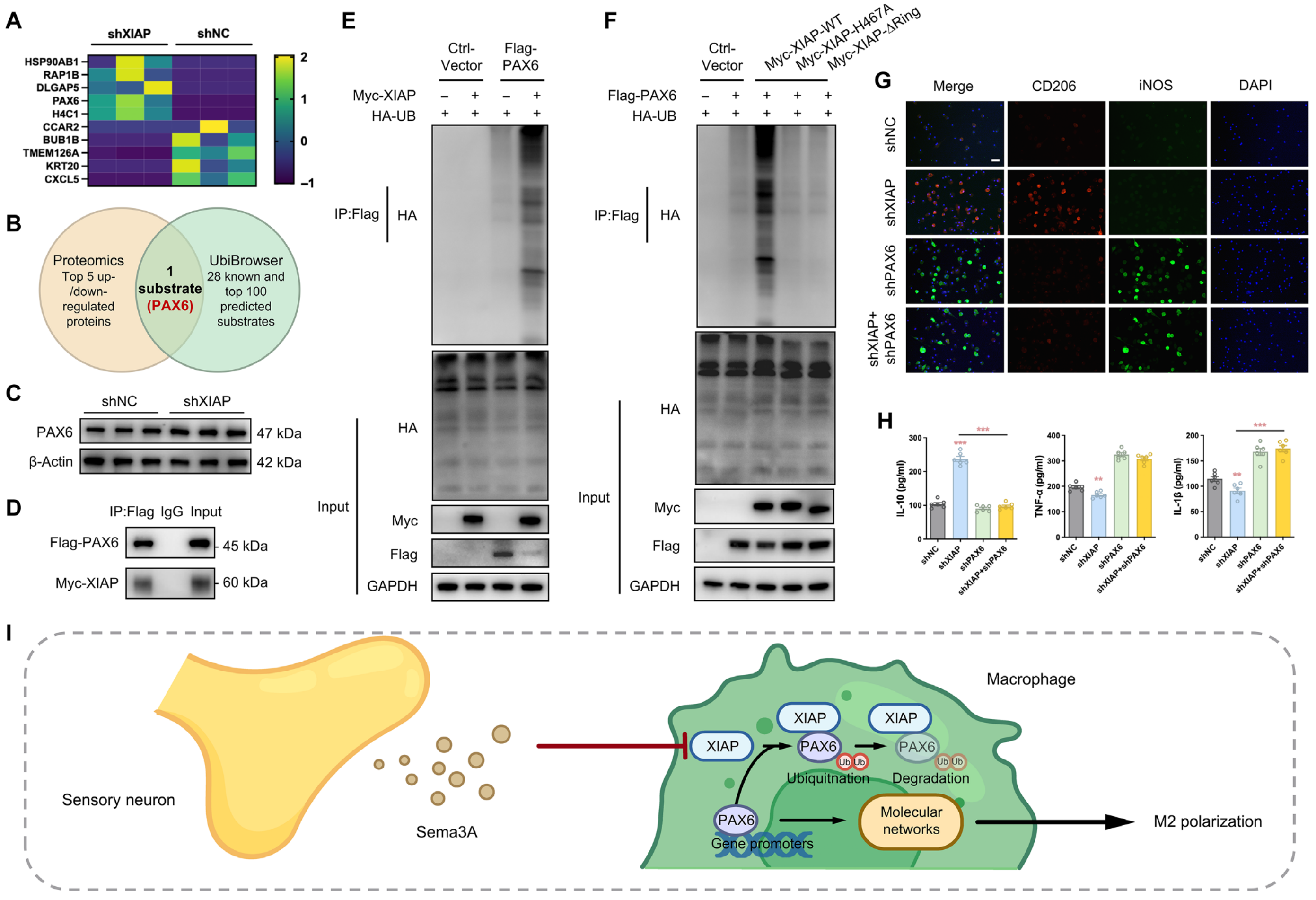

Fig. 9. XIAP-mediated PAX6 ubiquitination regulates macrophage polarization. (**A**) Heatmap of the top 5 proteins with up-regulated and down-regulated expression identified by proteomic analysis between macrophages with or without XIAP knockdown. (**B**) Overlap between selected proteomic results and the UbiBrowser database. PAX6 was the only overlapping protein. (**C**) Representative Western blotting images of PAX6 expression after XIAP knockdown. (**D**) Co-IP assay to analyze the interaction between XIAP and PAX6 after cotransfection of Myc-XIAP and Flag-PAX6 in HEK293T cells. (**E**) The ubiquitin level of PAX6 was detected in HEK293T cells using an IP assay after cotransfection by Myc-tagged XIAP (Myc-XIAP), Flag-tagged PAX6 (Flag-PAX6), and HA-tagged ubiquitin (HA-UB) plasmids. (**F**) HEK293T cells were transfected with plasmids of Myc-XIAP (WT, H467A, or ΔRing), Flag-PAX6, and HA-UB and then subjected to ubiquitin detection. (**G**) Immunofluorescence images of macrophages (expressing CD206 and iNOS) after knockdown of XIAP or PAX6 using shXIAP or shPAX6, respectively. (**H**) ELISAs of IL-10, TNF-α, and IL-1β. (**I**) Schematic diagram of the possible mechanism of macrophage polarization mediated by Sema3A via the Sema3A/XIAP/Pax6 pathway. $^{**}P < 0.01$; $^{***}P < 0.001$.

analysis further revealed that XIAP strongly coimmunoprecipitated with PAX6 (Fig. 9D). These results indicated that XIAP directly interacts with PAX6 and may promote its proteasomal degradation.

Next, we investigated the effect of XIAP on the ubiquitination of PAX6. Our findings showed that XIAP significantly increased PAX6 ubiquitination in HEK293T cells transfected with Myc-XIAP, Flag-PAX6, and hemagglutinin (HA)–tagged ubiquitin (HA-UB) plasmids (Fig. 9E). To further verify that the interaction of XIAP and PAX6 depended on the E3 ubiquitin ligase functional domain of the former, we generated a truncated mutant plasmid Myc-XIAP-ΔRing, and a mutant plasmid Myc-XIAP-H467A with active site deletion, according to a previous study (*81*), and cotransfected them into HEK293T cells. We observed that both H467A mutation and ΔRing truncated mutation of XIAP failed to catalyze the ubiquitination of PAX6 (Fig. 9F), indicating that the E3 ubiquitin ligase domain of XIAP was required for downstream PAX6 ubiquitination. Collectively, these results revealed that XIAP interacts with PAX6 and induces its ubiquitination for protein degradation.

It has been reported that PAX6 is closely involved in immune regulation. For instance, PAX6 knockdown leads to changes in the expression of downstream oxidative stress–related genes (*82*); it also activates Iba1-mediatied remodeling of microglial cells for immune surveillance in the nervous system (*83*). Therefore, we investigated the role of PAX6 degradation via ubiquitination in macrophage polarization. Immunofluorescence staining for CD206 and iNOS showed that the specific knockdown of PAX6 by shPAX6 transfection (fig. S29) resulted in a notable increase in the green signal of iNOS (Fig. 9G), suggesting increased macrophage transition to the M1 phenotype in the absence of PAX6. Moreover, PAX6 knockdown completely blocked the M2 polarization induced by XIAP knockdown (Fig. 9G). This phenomenon was also confirmed by the results of the ELISA of related cytokines (Fig. 9H). In addition, to verify the in vivo expression of PAX6 following application of the bone repair system, an immunofluorescence staining of PAX6 and CD68 (a common marker for macrophages) was conducted. The results indicated that the expression of PAX6 collocated with $CD68^+$ macrophages was significantly increased at 1 week after implantation of the M13-AV-NK/β-TCP/g-Col I hydrogel (fig. S30), which has been proved to induce M2 macrophage polarization in the above investigations (Fig. 6, D and E). Together, these results clarified that the degradation of PAX6 regulated by the XIAP-mediated ubiquitin-proteasome pathway plays a crucial role in promoting macrophage polarization toward the M1 phenotype (Fig. 9I).

Further prediction of the downstream target genes of PAX6 was performed using the Gene Transcription Regulation Database (GTRD) and the Cistrome Data Browser (CDB) database. Several genes, including *PDK1*, *TAZ*, and *Axin2*, were identified. These three molecules have been reported as key regulatory factors of the PI3K/Akt (*84*), Hippo/YAP (*85*), and Wnt (*86*) signaling pathways, respectively, all of which are closely involved in macrophage phenotype transition. Consequently, it is reasonable to speculate that PAX6 affects the transcription of multiple target genes to regulate downstream molecular networks, thereby mediating Sema3A-induced M2 polarization (Fig. 9I). However, the specific interaction mechanisms require further investigation.

DISCUSSION

There are some limitations in the present study. First, in vivo validation of the Sema3A/XIAP/PAX6 axis in sensory nerve–mediated macrophage polarization was limited as we only characterized the changes in PAX6 expression levels. For a more rigorous investigation, in vivo rescue experiments should be conducted in future studies to provide deeper insights. Second, the therapeutic effect of the phage-loaded hydrogel depends on the presence of residual sensory nerves around the bone defect area. In cases of severe nerve damage or complete denervation, the treatment is less effective. This suggests that the approach may not be suitable for patients with extensive nerve injuries, emphasizing the need for complementary strategies to transplant sensory nerves (*87*) into bone tissue engineering materials.

Collectively, this study highlighted the immunomodulatory role of sensory innervation in the early stage of repairing processes after tissue injury. To harness these neuroimmune regenerative modulations, we successfully constructed a sensory neuron–homing β-NGF–binding phage to specifically promote sensory nerve growth by recruiting free β-NGF in the microenvironment. On the basis of this dual-functional double-displayed phage, we fabricated a composite hydrogel system to allow long-term release of phages in the context of bone defect repair in vivo. The phage-loaded system specifically promoted sensory innervation and accelerated the transition of inflammation to the pro-repair stage to obtain a promising bone healing outcome. Mechanistically, sensory innervation altered the progression of inflammation by facilitating a temporal decrease in the M1/M2 ratio. Further investigations at the cellular level demonstrated that sensory neurons express Sema3A to inhibit XIAP-mediated PAX6 ubiquitination, subsequently inducing macrophage M2 polarization. Overall, this study presented a prospective phage-based strategy for selectively inducing sensory innervation and confirmed the perspective that sensory innervation temporally alleviates inflammation and accelerates tissue regeneration. Such specific regenerative treatments may have broader applications in addressing peripheral neuropathy, chronic wound healing, and other immunological diseases by using neuroimmune interactions.

MATERIALS AND METHODS

Animal model establishment and in vivo treatment

All animal and cell experimental protocols used in the present study were approved by the Ethics Committee for Animal Research, Second Affiliated Hospital, School of Medicine, Zhejiang University (no. AIRB-2023-1085). Eighty male Sprague-Dawley rats weighing 250 ± 10 g (6 to 8 weeks old) obtained from the Laboratory Animal Center of Zhejiang University were used in total. Rats were randomly divided into different groups for surgery or implantation ($n = 5$). No samples, rats, or data points were excluded. To evaluate the effects of sensory innervation on the physiological process of bone healing, a rat mandibular defect model combined with denervation of IAN was first established. Briefly, rats were anesthetized with an intraperitoneal injection of 2% pentobarbital sodium (0.2 ml/100 g), and their left maxillofacial regions were skinned and cleaned with iodine. After making a vertical incision, the medial muscles of mandible were bluntly dissected along the periosteum until the milky white IAN was exposed. A nerve segment was isolated from the proximal end of IAN to the edge of mandibular foramen and then carefully removed, with a length of 3 mm at least, to avoid self-repair of the nerve stump. Next, the lateral muscles of mandible were also separated in the same incision, and a full-thickness bone defect with 4 mm in diameter was trephined by electric drill in the flat area of mandibular angle, followed by suturing and a daily intraperitoneal injection of penicillin (400,000 units, ST488, Beyotime, China) for

3 consecutive days. Sham surgery was conducted for the control group with only IAN exposure, and bone defect, but no denervation.

To assess the in vivo neuroregulatory, immunomodulatory and osteogenic effects of the composite hydrogels with loaded dual-functional M13-AV-NK phages, a critical-sized mandibular defect with a diameter of 5 mm was prepared in this part. The procedure of the surgery was the same as the establishment of mandibular defect model as mentioned above, except that the diameter of the defects was 5 mm to avoid bone self-healing. Fifty microliters of the different hydrogels (β-TCP/Col I, M13-WT/β-TCP/Col I, and M13-AV-NK/β-TCP/Col I hydrogels) was then separately injected to fill the defect region by a syringe, before suturing. In addition, to further investigate the decisive effect of sensory nerve during the healing processes promoted by the composite hydrogels, IAN was denervated according to the above methods in another set of animal experiments, prior to making the critical-sized defect and injecting the M13-AV-NK/β-TCP/Col I hydrogel.

All rats were euthanized by an intraperitoneal injection of overdose pentobarbital sodium after 1, 2, and 8 weeks of operation or implantation. The mandibles were harvested and stored in 4% paraformaldehyde for further RNA-seq, micro-CT detection, and histological and immunohistochemical analysis. In addition, the heart, liver, lung, spleen, and kidney of rats were also collected at 8 weeks for histological analysis to ensure the in vivo biosecurity of composite hydrogels.

In addition, a rat dorsal subcutaneous implantation model was conducted to evaluate the degradation rate of the composite hydrogel systems in vivo. Briefly, after anesthesia, a transverse incision was made in the back skin of rats with a length of 3 to 5 mm. The subcutaneous tissues were carefully bluntly separated, and 100 μl of M13-AV-NK/β-TCP/g-Col I hydrogels was then injected into the subcutaneous tissue space, followed by suture. The hydrogels were collected at different time points (days 1, 3, 7, 14, and 28 after implantation), lyophilized, and weighed for assessment of the degradation rate.

RNA-seq and bioinformatics analysis

To investigate the physiological changes in local microenvironment after sensory denervation, the total RNA from the tissues surrounding the mandibular defect was extracted using TRIzol reagent (15596026, Invitrogen, USA) according to the manufacturer's instructions. In addition, the total RNA of DRGCs cultured with different phages plus periodically added exogenous β-NGF (100 ng/ml, 450-01, PeproTech, USA) (Fig. 4G) and macrophages cultured with recombinant Sema3A (100 ng/ml, HY-P78350, MCE, USA) for 48 hours was also extracted for sequencing to explore the potential molecular biological mechanisms. After RNA purification, reverse transcription, and library construction, RNA-seq was performed on NovaSeq X Plus platform (PE150) using the NovaSeq Reagent Kit at Majorbio Bio-pharm Biotechnology Co. Ltd. (Shanghai, China). The significant DEGs between samples were identified with $|\log_2 FC| \geq 1$ and $FDR < 0.001$ (DEGseq) or 0.05 (DESeq2). All of the data analysis, including functional-enrichment analysis of GO and KEGG pathway, was carried out on the Majorbio Cloud Platform (www.majorbio.com).

Micro-CT evaluation

The harvested mandibles were scanned with a micro-CT scanner (Heidelberglaan 100, MILabs BV, Utrecht) after being fixed in 4% paraformaldehyde solution for 72 hours. Scanning was performed with a resolution of 40 μm per pixel and an exposure time of 75 ms at 55 kV/0.17 mA, and 1440 projections were collected in total. All samples were wrapped in paper soaked in phosphate-buffered solution (PBS) to avoid dehydration when scanning. The software (Imalytics Preclinical 2.1) associated with the scanner was used for reconstruction of sections with a low-pass Gaussian filter (stddev = 1.0) and a standardized threshold (>1600 HU). Then, the defect in the area of mandibular angle was identified by a cylindrical region of interest, and two indicators (defect coverage percentage and new bone volume) were calculated for quantitative analysis to characterize the bone repair effect (fig. S31).

Histological analysis

After micro-CT scanning, all fixed mandibular tissues were decalcified with 10% EDTA solution (pH 7.4, 0105, Amresco, USA) for a duration of 20 days, followed by dehydration in 30% sucrose and embedding in paraffin. Coronal-oriented sections with a thickness of 8 μm were then prepared and stained with H&E, as well as Masson's trichrome. TRAP staining was also used to label activated osteoclasts. In addition, tissues from the heart, lung, liver, kidney, and spleen of rats were also collected for H&E staining to confirm the absence of any in vivo adverse effects resulting from the different composite hydrogels.

For immunohistochemistry analysis, slides of each tissue underwent processing with primary antibodies against CGRP (1:1000, ab283568, Abcam, UK), Dopamine (1:2000, ab209487, Abcam), iNOS (1:2000, ab283655, Abcam), CD206 (1:5000, ab64693, Abcam), ALP (1:1000, ab65834, Abcam), and OCN (1:1000, AB10911, Sigma-Aldrich, USA), followed by incubation of the corresponding secondary antibodies conjugated to horseradish peroxidase (HRP). All these slides were subjected to observation and imaging via a light microscopy (Aperio GT 450, Leica, GER) and were reviewed in a blinded manner by another histologist.

For immunofluorescence staining, slides of each tissue were stained using the TSAPlus fluorescence staining kit (G1259, Servicebio, China), according to the manufacturer's instructions, with the following primary antibodies: TUBB3 antibody (1:2000, ab215037, Abcam), CGRP antibody (1:1000, ab283568, Abcam), Dopamine antibody (1:2000, ab209487, Abcam), CD68 antibody (1:2000, ab125212, Abcam), iNOS antibody (1:2000, ab283655, Abcam), CD86 antibody (1:500, ab238468, Abcam), CD206 antibody (1:5000, ab64693, Abcam), CD163 antibody (1:500, ab182422, Abcam), CD31 antibody (1:2000, ab182981, Abcam), Sema3A antibody (1:1000, 27836-1-AP, Proteintech, USA), and PAX6 (1:1000, 67529-1-Ig, Proteintech). 4′,6-Diamidino-2-phenylindole (DAPI; ab228549, Abcam) was used to label the cell nucleus. The staining results were imaged by a confocal laser scanning microscope (CLSM; Olympus FV1000) and quantified by ImageJ software.

Flow cytometry

To evaluate the in vivo macrophage polarization induced by sensory nerve denervation or composite hydrogel implantation, the callus was isolated from bone defect area in mandible at 1, 2, or 4 weeks after surgery, diced, and digested for 60 min at 37°C and 150 rpm in haluronidase (0.2 mg/ml; H8030, Solarbio, China) plus collagenase II (2 U/ml; C8150, Solarbio) in serum-free α-MEM medium. After digestion, the suspension was filtered through a 70-μm cell strainer (Beckman, USA) and treated with red blood cell lysis buffer (R1010, Solarbio). The cytokine staining was performed according to the standard protocols, including fixation and permeabilization with a BD CytoFix/CytoPerm Kit (554714, BD Biosciences, USA). The stained cells were detected by a CytoFLEX flow cytometer (Beckman, USA), and the results were analyzed by FlowJo Flow Cytometry Analysis Software (Tree Star). The macrophage panels displayed in this study include Zombie (423101, BioLegend, USA), CD68 (bs-20403R-Cy3, Bioss, China), CD86 (200314, BioLegend), and CD206 (bs-4727R-FITC, Bioss).

Cell isolation and culture

Isolation of DRGs

DRGs were isolated and cultured by standardized method. Briefly, a midline longitudinal incision on the back of newborn rats was performed after euthanasia by intraperitoneal injection of pentobarbital sodium to fully expose the spine and then the spinal cord. Round and chrome yellow DRGs were visualized near the intervertebral foramen and extracted using microtweezers. The redundant nerve roots of dissected DRGs were carefully removed under a stereomicroscope, followed by digestion with 0.25% trypsin for 5 min and soak in Dulbecco's modified Eagle's medium (DMEM) complete medium. Next, DRGs were transferred to a confocal dish and cultured in a neurobasal medium (21103049, Invitrogen) containing 0.3% L-glutamine and β-NGF (100 ng/ml; 450-01, PeproTech) for further investigations.

Isolation and culture of DRGCs

The initial steps of DRGCs isolation were the same as DRGs isolation described above. After dissection, separated DRGs were washed twice with PBS, following sequential digestion with 0.2% collagenase II at 37°C for 30 min and 0.25% trypsin for another 15 min. Then, the DMEM/F12 complete medium was added to terminate the trypsin reaction, and the cell pellets were suspended after centrifugation. DRGCs were incubated in a dish precoated with poly-D-lysine (A3890401, Invitrogen) at 37°C and 5% CO_2 for first day, and the medium was replaced with the DRGC complete medium (CM-R126, Procell, China) with additional cytarabine (5 μM, MedChemExpress, USA) on the next day to inhibit the growth of other nonneuronal cells. On the third day, the culture medium was changed to the pure DRGC complete medium and updated every 3 days until further investigations.

For encapsulation of DRGCs in hydrogels to assess the biocompatibility of the repairing system, cells were carefully digested and mixed with pre-hydrogel solutions at a density of 1×10^6 cells ml^{-1}, which were then seeded onto a cover slide and incubated at 37°C for at least 30 min to allow a sufficient solution-to-gelation transition process. After gelation, complete culture medium was additionally replenished and the DRGCs/hydrogel composites were cultured for 24 hours before further viability assay.

Isolation and culture of BMDMs

BMDMs were isolated from 6-week-old C57BL/6 mice, which were first anesthetized by 2% pentobarbital sodium via intraperitoneal injection and euthanized by cervical dislocation. The femurs and tibias were then isolated aseptically and the marrow cavities were completely exposed, followed by flushing and collecting the bone marrow tissues using α-MEM culture medium (12571063, Gibco, USA). After lysis of red blood cells using ACK lysis buffer (R1010, Solarbio), BMDMs were seeded in a flask with complete culture medium containing macrophage colony-stimulating factor (30 ng/m; 315-02, PeproTech). The cells were cultured at 37°C in a humidified atmosphere of 5% CO_2 and detached on the fifth day of plating for subsequent experiments.

Besides, conditioned culture of primary macrophages was performed to determine the polarization effects caused by sensory neurons. The supernatant from DRGCs was collected after 3 days of culture, centrifuged and mixed with complete culture medium of BMDMs at a 1:1 ratio to get the CM. The BMDMs were then cultured with this CM until further investigations. To verify the significant role of Sema3A in macrophage polarization, recombinant Sema3A (100 ng/ml) was added into the CM collected from Sema3A knockdown DRGCs for observing the phenotype change of BMDMs.

Cell transfection

To down-regulate the expression of specific protein, shSema3A (GenScript Biotech, Nanjing, China) for DRGCs, shXIAP and shPAX6 (GenScript Biotech) for BMDMs were synthesized and transfected into the corresponding cells using Lipofectamine 2000 (11668027, Invitrogen) following the manufacturer's instructions. Cells treated with shNC were seen as the control. The short hairpin RNA sequences were listed in table S2. To up-regulate the expression of XIAP in BMDMs, cells were transfected with the pcDNA3.1-XIAP plasmid or the empty pcDNA3.1 vector, cultured for 48 hours, and reaped for further study. The transfection efficiency was confirmed by Western blot analysis. For ubiquitination-related experiments, HEK293T cells (SNL-015, SUNNCELL, China) were used and cultured in DMEM complete medium containing 1% penicillin/streptomycin (V900929, Sigma-Aldrich) in 5% CO_2 at 37°C. Plasmids of Flag-PAX6, Myc-XIAP, and its mutants were purchased from miaolingbio (Wuhan, China), and ubiquitin was cloned into the pcDNA3.1-HA vector. Transfection of 293T cells was conducted according to the standard protocol.

Phage display

In vitro phage display was conducted according to the standardized protocol (Fig. 3A). Briefly, a library of M13 phages displaying random 9-nucleotide oligomer peptides (termed PH.D.-9, obtained from Abiocenter Biotechnology Co. Ltd., Jiangsu, China) in the amount of at least 1×10^{12} transducing units was cocultured with rat Schwann cells (CP-R111, Procell) as a round of negative selection for 30 min to remove the phages recognizing non-DRGCs. After that, the supernatant containing unbound phages was collected and applied to interact with DRGCs for 1.5 hours of incubation in a humidified container at room temperature for positive panning. Then, the cells were rinsed eight times with wash buffer to completely remove the DRGCs-unbound phages, and the remained DRGCs-bound phages were eluted with an elution buffer and amplified using *E. coli* host strain XL1-Blue according to the standard experimental protocols. Titering of the amplified phages and ELISA detection were conducted before the next round of biopanning. The optical density (OD) value detected in ELISA being at least 0.5 higher than that of the blank control was considered to be a positive screening result. A total of five rounds of positive biopanning were performed, and 104 random phage clones were selected for DNA sequencing from the fourth and fifth screening. The peptide sequences in each round of selection were deduced from the DNA sequence.

For phage amplification, the eluate solution was first mixed with XL1-Blue (OD value at 0.8 to 1.0) and incubated at room temperature for 30 min. The resultant phage-infected bacteria were then cultured at 37°C and 250 rpm stirring for 30 min, followed by addition of helper phages in the amount of 2×10^{10} PFU and afterward another 1 hour at 250 rpm. After amplification, the mixture of phages and bacteria was centrifuged at 7200*g* for 10 min, and the supernatant was transferred into a sterile flask and incubated with NaCl/polyethylene glycol (PEG) [2.5 M NaCl and 16.7% PEG-8000 (PEG, molecular weight 8000)] at 4°C overnight for phage precipitation. The phage solution was centrifuged the next day at 13,000*g* for 1 hour and resuspended with PBS for further biopanning or other investigations.

For titering of phages, the phage solution was diluted in a 1:10 volume ratio and mixed with XL1-Blue *E. coli* at mid-log phase ($OD_{600} = 0.5$) for 5 min of incubation at room temperature. The solution mixture was then transferred into top agar preheated at 45°C, immediately vortexed, and spread onto a prewarmed LB/IPTG/Xgal plate, followed by mildly shaking to evenly distribute the top agar. After 5 min of cooling, the plate was inverted and placed in a constant temperature incubator at 37°C overnight. The titer of phages was calculated by the counts of plaque on the plate (titer $= N \times D$ PFU/ml, where N and D represent the number of plaques and the dilution ratio, respectively).

Enzyme-linked immunosorbent assay

To verify the affinity of the selected phages displaying AV or NK peptide toward the sensory neurons and β-NGF, respectively, phage ELISA experiments were conducted. Briefly, DRGCs or β-NGF (diluted in coating buffer) were first immobilized in a plate and blocked with a blocking buffer. Approximately 10^9 PFU of phages were then added into the plate wells and incubated for 1 hour at 4°C, followed by incubation of anti-phage coat protein g8p antibody (ab9225, Abcam) and HRP-labeled goat anti-mouse secondary antibody (ab6789, Abcam) at 4°C for an hour each. The color reaction was done by the TMB ELISA substrate (ab171523, Abcam), and the absorbance of each well was detected at 450 nm by a spectrophotometer (Shimadzu UV-3150).

For assessment of in vivo inflammation activity in the bone defect area after surgery or implantation, the concentrations of inflammation-related cytokines TNF-α and IL-10 in the callus of bone defect were determined by the relevant ELISA kits (Neobioscience Technology, Hong Kong, China), referring to the manufacturer's instructions. The supernatants of macrophages cultured with various treatments were also collected to investigate the concentration of IL-10, IL-1β, and TNF-α by performing ELISA kits (Neobioscience Technology, Hong Kong). In addition, the CGRP ELISA kit (BIOESN, Shanghai, China) was used to determine the concentration of CGRP in the DRGCs-derived CM.

Evaluation of binding affinity of phages

To verify the in vitro binding affinity of phages displaying sensory neuron–targeting peptide, DRGCs or PC-12 cells were first incubated with different phages for 24 hours to allow the specific binding between sensory neurons and the phages. After fixation, cells were blocked and incubated with TUBB3 antibody (1:100, A18132, Abclonal) or Tyrosine Hydroxylase antibody (1:100, A12756, Abclonal) at 4°C for 8 hours, followed by incubation of secondary antibody and FITC-labeled M13 antibody (1:100, 11973-MM05T-F, SinoBiological, China) at the same time for another 2 hours. The cell nucleus was labeled by DAPI. The results were imaged by a CLSM (Olympus FV1000) and quantified by ImageJ software.

For in vivo evaluation of the binding affinity of M13-AV-NK phages toward β-NGF, the mandible samples with implantation of different hydrogels were collected at 1 week after surgery, fixed, decalcified, followed by incubation in 30% sucrose and embedded in Tissue-Tek. The samples were cut into 8-μm-thick sections. The slides were incubated with NGFB antibody (1:500, bs-0067R, Bioss) overnight at 4°C and then incubated with secondary antibody and FITC-labeled M13 antibody (1:100, 11973-MM05T-F, SinoBiological). The following steps are the same as the in vitro evaluation as mentioned above.

Computational studies of β-NGF–binding peptide

The 3D structure of β-NGF protein was simulated by the I-TASSER online server (https://zhanggroup.org/I-TASSER/), and the Cα-Cβ-side group protein model (CABS)-docking web server (http://biocomp.chem.uw.edu.pl/CABSdock/) was next used to generate the peptide-protein complex model to search for the potential binding sites between NK peptide and β-NGF. The best docking model from CABS-dock results was chosen based on cluster density and the avg-RMSD and set as the initial structure. Then, GROMACS software (http://www.mdtutorials.com/) was used to perform a 50-ns MD simulation at 10-ns intervals, drawing the relative stability of interaction between the β-NGF–binding peptide and β-NGF protein.

Construction of genetically engineered sensory neuron–homing β-NGF–binding phages

To achieve selective promotion of sensory nerves, we displayed the screened sensory neuron–homing peptide AV in the pIII region on the tip of the M13 phage and the reported β-NGF–binding peptide NK in the pVIII region on the side surface of the same phage to obtain a dual-functional phage. First, the NK peptide was fused to the corresponding site. Briefly, a pair of complementary nucleotides (5′-CCGTGGCCCAAGCGGCCAACGAACGTGCACTGACT-CTGGGCGAAGAAGGCGCAGTGG-3′ and 5′-TGATGGCCGAC-GGGGCCTTTAACCACTGCGCCTTCTTCGCCCAGAGT-CAGTGCACGTTC-3′) were designed and used for amplifying and forming double-stranded DNA fragments by PCR. Meanwhile, the Pcomb3x phage vector was digested by restriction endonuclease SfiI for 30 min at 50°C, followed by purification via agarose gel electrophoresis. The purified vector was then ligated with the previously annealed DNA fragment using T4 DNA ligase at 22°C for 40 min to obtain the recombinant plasmid (p-M13-NK), which could encode the NK peptide on pVIII of the M13 phage. After that, the p-M13-NK plasmids were transferred into the competent XL1-Blue bacterial cells, and the transfected cells subsequently underwent accurate heat shock, cooling, and plate cultivation. The positive clones of XL1-Blue were then picked up for DNA sequencing to verify the correct fusion of the β-NGF–binding peptide. Next, to simultaneously display the AV peptide on pIII, the correct XL1-Blue clones got in the preceding step were collected and used for amplification of the recombinant p-M13-NK plasmids by culturing in LB medium for 12 hours at 37°C in a shaker. The plasmids were then extracted using a GeneJET Plasmid Miniprep Kit (K0502, Invitrogen), digested by corresponding restriction endonucleases, and purified via agarose gel electrophoresis. After ligation of the annealed fragment and the p-M13-NK vector using T4 DNA ligase, a double-displayed recombinant plasmid (p-M13-AV-NK) was formed, encoding the AV and NK peptides fused to the pIII and pVIII regions of the M13 phages, respectively. The following procedures were similar to those described above, including transformation of plasmid into the competent cells and verification by DNA sequencing. In addition, nucleic acid electrophoresis was used to further ensure the success construction of the double-displayed phages. Briefly, the DNA of phages was extracted using a Phage DNA Isolation Kit (NGB-46800, Norgen Biotek, CA) according to the manufacturer's instructions and the electrophoresis was conducted by the standard method. All this part of experiments was performed with the technical support from Abiocenter Biotechnology Co. Ltd..

Cell viability assay

The biocompatibility of the dual-functional phages and the composite hydrogel systems was determined by a live/death cell staining kit (C2015M, Beyotime). Three groups of phage were set, including PBS (as the blank control), M13-WT, and M13-AV-NK. Briefly, DRGCs were cultured with phages, or within the corresponding composite hydrogels composed of phage, β-TCP, and Col I hydrogels for 24 hours, and then stained using the kit according to the manufacturer's protocol. The results were observed by a CLSM.

Functional evaluation of the double-displayed phages

To verify the in vitro promoting effect of the double-displayed M13-AV-NK phages on sensory nerve growth, DRGCs and DRG explants were first incubated with different phages for 2 hours and then washed with PBS to remove unbound phages. Next, exogenous β-NGF (100 ng/ml) was additionally added into the complete medium. Cells and explants were cultured with this extra β-NGF for 6 hours to allow the sufficient binding between the bound phages and free β-NGF, which was then replaced with normal neurobasal medium for washing away the unattached β-NGF. These steps of β-NGF treatment were performed once a day for a total of 3 days, followed by further evaluations (Fig. 4H).

Specifically, the growth of DRGCs was determined by immunofluorescence staining of CGRP and qRT-PCR of characteristic sensory neuron–related markers. For assessing the neurite branching and axon growth of DRGs, neurofilament staining was conducted, combined with Sholl analysis and axon analysis (Fig. 4I). Briefly, after manual definition of DRG center in the staining image, concentric circles spaced 10 μm apart were identified, and binarized traces of axons were created by using the "Sholl analysis" plugin in ImageJ (National Institutes of Health, Bethesda, MD, USA). Then, quantification of the trace lengths was conducted using the Simple Neurite Tracer for axon length analysis in ImageJ.

Immunofluorescence staining

For in vitro investigations, immunofluorescence staining was performed using standard protocol. Briefly, cells or explants were fixed and permeabilized with 0.4% Triton X-100 (T8200, Solarbio) and then blocked with 1% bovine serum albumin (A8010, Solarbio) and 2% goat serum for 1 hour. Next, cells or explants were incubated with the primary antibodies, including TUBB3 antibody (1:100, A18132, Abclonal, China), CGRP antibody (1:100, A5542, Abclonal), iNOS antibody (1:100, ab210823, Abcam), CD206 antibody (1:100, ab64693, Abcam), and Sema3A antibody (1:200, 27836-1-AP, Proteintech) followed by further incubation with corresponding secondary antibodies in the dark for 1 hour and DAPI for another 5 min. The staining results were imaged by a CLSM (Olympus FV1000) and quantified by ImageJ software.

Quantitative reverse transcription polymerase chain reaction

Total RNA of DRGCs was purified using TRIzol to assess the expression of sensory nerve marker genes *Cgrp* and *Tac1*. We performed qRT-PCR by the ChamQ Universal SYBR qPCR Master Mix (Q711-02, Vazyme, China) on an ABI StepOnePlus system (Applied Biosystems, Warrington, UK). Amplification of glyceraldehyde-3-phosphate dehydrogenase (GAPDH) was used as an internal control. The primer sequences used for this analysis are provided in table S3.

Construction of double-displayed phage-loaded hydrogels

The double-displayed phage-loaded hydrogels were mainly prepared by phages, β-TCP, and Col I solution (extracted from rat tail, 354249, Corning, ≈10 mg/ml). The whole scaffold fabrication processes are shown in Fig. 5 (A and B). Briefly, β-TCP (0.5 mg/ml) was obtained via a chemical precipitation method according to a previous study (*53*) and mixed with amplified M13-AV-NK phages at a titer of 1×10^{10} PFU/ml of the latter. The compound of phages and β-TCP was incubated in a shaker at 4°C overnight to allow sufficient attachment between these two compositions and subsequently centrifuged to collect the phage-loaded β-TCP complex. Next, for preparing the pre-hydrogel solution, the Col I solution first underwent pH adjustment to the physiological range (pH = 7.35 to 7.45) by 0.1 M sodium hydroxide solution and hydrochloric acid solution and was then adjusted to a physiological isotonic state using 10× PBS. After these two steps, the prepared M13-AV-NK/β-TCP particles were added into the pre-hydrogel solution at a mass ratio of 1:2, followed by mixture of 2% (v/v) genipin solution (0.01 g/ml, G101204, Aladdin, China) to cross-link the collagen fibers. Last, the fully mixed solutions were placed into a constant temperature incubator (37°C for about 30 min) for solution-to-gelatin transition to form the M13-AV-NK/β-TCP/ Col I hydrogels. In addition, PBS and M13-WT phages were added as the substitutes for M13-AV-NK phages to form the β-TCP/ Col I and M13-WT/β-TCP/ Col I hydrogels, respectively, for comparison. All the above steps were performed under aseptic conditions.

Detection of released phages from the composite hydrogels

To detect the release of loaded phages from the composite hydrogels, M13-AV-NK/β-TCP/Col I hydrogels were soaked in a buffer with 0.15 M NaCl and 200 mM NaH_2PO_4 (pH = 7) at 4°C. The supernatant containing the released phages was carefully collected at days 1, 3, 7, 14, and 28, followed by addition of new buffer into the original composite systems every time for allowing subsequent stable phage release. Then, phage tittering and bacterial plate cultivation were conducted for direct or indirect detection of phage concentrations (Fig. 5D). The steps of titering by plaque counting were the same as described above. For plate cultivation, *E. coli* was treated with the released phages on a constant temperature shaker at 37°C for 2 hours. After that, the bacteria suspensions were serially diluted and evenly spread on agar plates, following incubation in a constant temperature bacterial incubator at 37°C overnight. The plates were photographed by a camera, and the colony numbers on the surface of each agar plate were counted using ImageJ. In addition, the same experiments were performed using M13-AV-NK/Col I hydrogels as an alternative to clarify the slow-release effect caused by β-TCP.

For assessing the in vivo phage release efficiency of the composite hydrogels, the implanted M13-AV-NK/β-TCP/Col I hydrogels were collected at different time points, including days 1, 3, 7, 14, and 28 after implantation from the bone defect area. The harvested hydrogels were fixed and incubated with FITC-labeled M13 antibody (1:100, 11973-MM05T-F, SinoBiological) for 2 hours at room temperature and then observed using a CLSM (Olympus FV1000) and quantified by ImageJ software.

Characterization of the composite hydrogels

Dynamic light scattering

To assess the particle size distribution and PdI, β-TCP was measured using a DLS instrument (Zetasizer Nano ZS, Malvern Panalytical, UK).

Transmission electron microscopy

TEM (JEM-1400flash, Japan) was conducted to visualize the ultrastructure of M13 phages and β-TCP, as well as the attachment between these two. Samples were carefully added onto the grid using a pipette gun, following negative staining by 2% uranium acetate. The grids were allowed to air-dry completely before being transferred into the TEM chamber, and images were acquired at an accelerating voltage of 80 kV.

Attenuated total reflectance–Fourier transform infrared spectroscopy

ATR-FTIR spectrometer (Nicolet 5700, USA) was applied to detect the infrared radiation spectrum of different hydrogels to monitor the genipin-induced cross-linking process. Five groups were set in this part, including Col I, g-Col I, PBS/β-TCP/g-Col I, WT/β-TCP/g-Col I, and AV-NK/β-TCP/g-Col I. The measurement was carried out in transmittance mode for 75 scans in total, from 500 to 4000 cm^{-1} at a wave number resolution of 5 cm^{-1} at room temperature.

Mechanical properties measurements

Groups were the same as described above in the "Attenuated total reflectance–Fourier transform infrared spectroscopy" section. Briefly, for determining the mechanical properties of different hydrogels after gelation, a rotational rheometer (RS6000, Hake, Germany) was applied with test parameters of 1 Hz and 1% strain.

Scanning electron microscopy

The microtopography of different composite hydrogels was examined using SEM (SU-8010, Hitachi, Japan). Samples were fixed in 2.5% glutaraldehyde (P1126, Solarbio) overnight and underwent a progressive dehydration process in a series of graded alcohol solutions (concentrations ranging from 30 to 100%) with at least 15 min for each concentration step. Then, samples were dried by a critical point drying method (Hcp-2, Hitachi), mounted on an aluminum stub with gold sputter coating (Hitachi E-1010), and subsequently observed under SEM at an accelerating voltage of 3.0 kV. For cellular hydrogel sample, DRGCs were cultured on the surface of corresponding composite hydrogel for 24 hours and underwent the same protocols as described above before imaging.

Western blotting analysis and Co-IP

Western blotting was performed to elucidate the change of protein expression levels. Briefly, cells were lysed by radioimmunoprecipitation assay lysis buffer (AIWB-012, Affinibody LifeScience, China) containing an inhibitor cocktail (87785, Thermo Fisher Scientific, USA), and the total proteins were separated by SDS–polyacrylamide gel electrophoresis gel after determining the concentration using a bicinchoninic acid (BCA) reagent (P0009, Beyotime) and transferred to polyvinylidene fluoride membranes (Merck Millipore, Billerica, MA). The membranes were then blocked with 5% skim milk for 1 hour and incubated with specific primary antibodies followed by an HRP-labeled secondary antibody. Last, HRP signals were detected using an enhanced chemiluminescence method (Amersham Biosciences) reaction solution (36208-A, Yeasen, China). With regard to Co-IP, an IP buffer (87787, Thermo Fisher Scientific) containing the inhibitor cocktail was used for protein extraction. The lysates were incubated with the corresponding antibodies and protein-A/G magnetic beads (B23201, Bimake, China) at 4°C with gentle rocking overnight. The beads were washed with an appropriate amount of lysis buffer, then eluted, and analyzed by immunoblotting.

The antibodies used in this part of experiments include Sema3A (1:1000, 27836-1-AP, Proteintech), MMP13 (1:2000, 181651-AP, Proteintech), XIAP (1:2000, A20846, Abclonal), PAX6 (1:500, A19099, Abclonal), β-actin (1:100000, AC026, Abclonal), Flag-Tag (80010-1-RR, Proteintech), Myc-Tag (60003-2-Ig, Proteintech), HA-Tag (#2367, Cell Signaling Technology, USA), and anti-rabbit/mouse-HRP (BA1056, Boster, USA).

Proteomic analysis

BMDMs were collected after specific knockdown of XIAP by transfection with shXIAP plasmid and shNC as the control. The proteins were extracted according to the manufacturer's instructions, cryopreserved, and sent for a TMT-based quantitative proteomics experiment. Samples were analyzed by liquid chromatography–tandem mass spectrometry, and the data analysis was carried out by using the Sangerbox online platform (www.sangerbox.com).

Statistical analysis

All data are presented as the means ± SD from at least three independent experiments. Statistical analyses were performed using GraphPad Prism 10 (GraphPad Inc., San Diego, CA). One-way analysis of variance (ANOVA) with the Tukey's post hoc test or Student's *t* test was conducted to calculate significant differences between groups. Also, $P < 0.05$ was considered as a statistically significant difference for all comparisons.

Supplementary Materials

This PDF file includes:
Figs. S1 to S31
Tables S1 to S3

REFERENCES AND NOTES

1. I. Rajpar, R. E. Tomlinson, Function of peripheral nerves in the development and healing of tendon and bone. *Semin. Cell Dev. Biol.* **123**, 48–56 (2022).
2. R. Tao, B. Mi, Y. Hu, S. Lin, Y. Xiong, X. Lu, A. C. Panayi, G. Li, G. Liu, Hallmarks of peripheral nerve function in bone regeneration. *Bone Res.* **11**, 6 (2023).
3. A. Kumar, J. P. Brockes, Nerve dependence in tissue, organ, and appendage regeneration. *Trends Neurosci.* **35**, 691–699 (2012).
4. Z. Guan, W. Yuan, J. Jia, C. Zhang, J. Zhu, J. Huang, W. Zhang, D. Fan, H. Leng, Z. Li, Y. Xu, C. Song, Bone mass loss in chronic heart failure is associated with sympathetic nerve activation. *Bone* **166**, 116596 (2023).
5. L. Rabiller, E. Labit, C. Guissard, S. Gilardi, B. P. Guiard, L. Moulédous, M. Silva, G. Mithieux, L. Pénicaud, A. Lorsignol, L. Casteilla, C. Dromard, Pain sensing neurons promote tissue regeneration in adult mice. *NPJ Regen. Med.* **6**, 63 (2021).
6. H. Chen, B. Hu, X. Lv, S. Zhu, G. Zhen, M. Wan, A. Jain, B. Gao, Y. Chai, M. Yang, X. Wang, R. Deng, L. Wang, Y. Cao, S. Ni, S. Liu, W. Yuan, H. Chen, X. Dong, Y. Guan, H. Yang, X. Cao, Prostaglandin E2 mediates sensory nerve regulation of bone homeostasis. *Nat. Commun.* **10**, 181 (2019).
7. G. Hoeffel, G. Debroas, A. Roger, R. Rossignol, J. Gouilly, C. Laprie, L. Chasson, P. V. Barbon, A. Balsamo, A. Reynders, A. Moqrich, S. Ugolini, Sensory neuron-derived TAFA4 promotes macrophage tissue repair functions. *Nature* **594**, 94–99 (2021).
8. A. E. Dubin, A. Patapoutian, Nociceptors: The sensors of the pain pathway. *J. Clin. Invest.* **120**, 3760–3772 (2010).
9. C. Chu, D. Artis, I. M. Chiu, Neuro-immune interactions in the tissues. *Immunity* **52**, 464–474 (2020).
10. K. Maruyama, Y. Takayama, T. Kondo, K. I. Ishibashi, B. R. Sahoo, H. Kanemaru, Y. Kumagai, M. M. Martino, H. Tanaka, N. Ohno, Y. Iwakura, N. Takemura, M. Tominaga, S. Akira, Nociceptors boost the resolution of fungal osteoinflammation via the TRP channel-CGRP-Jdp2 axis. *Cell Rep.* **19**, 2730–2742 (2017).
11. D. Yang, A. Jacobson, K. A. Meerschaert, J. J. Sifakis, M. Wu, X. Chen, T. Yang, Y. Zhou, P. V. Anekal, R. A. Rucker, D. Sharma, A. Sontheimer-Phelps, G. S. Wu, L. Deng, M. D. Anderson, S. Choi, D. Neel, N. Lee, D. L. Kasper, B. Jabri, J. R. Huh, M. Johansson,

J. R. Thiagarajah, S. J. Riesenfeld, I. M. Chiu, Nociceptor neurons direct goblet cells via a CGRP-RAMP1 axis to drive mucus production and gut barrier protection. *Cell* **185**, 4190–4205.e25 (2022).
12. Y.-Z. Lu, B. Nayer, S. K. Singh, Y. K. Alshoubaki, E. Yuan, A. J. Park, K. Maruyama, S. Akira, M. M. Martino, CGRP sensory neurons promote tissue healing via neutrophils and macrophages. *Nature* **628**, 604–611 (2024).
13. M. Karin, H. Clevers, Reparative inflammation takes charge of tissue regeneration. *Nature* **529**, 307–315 (2016).
14. S. A. Eming, T. A. Wynn, P. Martin, Inflammation and metabolism in tissue repair and regeneration. *Science* **356**, 1026–1030 (2017).
15. C. Nathan, Points of control in inflammation. *Nature* **420**, 846–852 (2002).
16. R.-R. Ji, A. Chamessian, Y.-Q. Zhang, Pain regulation by non-neuronal cells and inflammation. *Science* **354**, 572–577 (2016).
17. M. Tamari, K. L. Del Bel, A. M. Ver Heul, L. Zamidar, K. Orimo, M. Hoshi, A. M. Trier, H. Yano, T. L. Yang, C. M. Biggs, K. Motomura, R. Shibuya, C. D. Yu, Z. Xie, H. Iriki, Z. Wang, K. Auyeung, G. Damle, D. Demircioglu, J. K. Gregory, D. Hasson, J. Dai, R. B. Chang, H. Morita, K. Matsumoto, S. Jain, S. Van Dyken, J. D. Milner, D. Bogunovic, H. Hu, D. Artis, S. E. Turvey, B. S. Kim, Sensory neurons promote immune homeostasis in the lung. *Cell* **187**, 44–61.e17 (2024).
18. A. Marrella, T. Y. Lee, D. H. Lee, S. Karuthedom, D. Syla, A. Chawla, A. Khademhosseini, H. L. Jang, Engineering vascularized and innervated bone biomaterials for improved skeletal tissue regeneration. *Mater. Today (Kidlington)* **21**, 362–376 (2018).
19. L. Claes, S. Recknagel, A. Ignatius, Fracture healing under healthy and inflammatory conditions. *Nat. Rev. Rheumatol.* **8**, 133–143 (2012).
20. I. Němec, V. Smrčka, J. Pokorný, The effect of sensory innervation on the inorganic component of bones and teeth; experimental denervation - Review. *Prague Med. Rep.* **119**, 137–147 (2018).
21. M. Wu, L. J. Hill, L. E. Downie, H. R. Chinnery, Neuroimmune crosstalk in the cornea: The role of immune cells in corneal nerve maintenance during homeostasis and inflammation. *Prog. Retin. Eye Res.* **91**, 101105 (2022).
22. Y. Zhang, J. Xu, Y. C. Ruan, M. K. Yu, M. O'Laughlin, H. Wise, D. Chen, L. Tian, D. Shi, J. Wang, S. Chen, J. Q. Feng, D. H. Chow, X. Xie, L. Zheng, L. Huang, S. Huang, K. Leung, N. Lu, L. Zhao, H. Li, D. Zhao, X. Guo, K. Chan, F. Witte, H. C. Chan, Y. Zheng, L. Qin, Implant-derived magnesium induces local neuronal production of CGRP to improve bone-fracture healing in rats. *Nat. Med.* **22**, 1160–1169 (2016).
23. Z. Li, C. A. Meyers, L. Chang, S. Lee, Z. Li, R. Tomlinson, A. Hoke, T. L. Clemens, A. W. James, Fracture repair requires TrkA signaling by skeletal sensory nerves. *J. Clin. Invest.* **129**, 5137–5150 (2019).
24. V. S. Rana, C. Kitsou, S. Dutta, M. H. Ronzetti, M. Zhang, Q. Bernard, A. A. Smith, J. Tomás-Cortázar, X. Yang, M. J. Wu, O. Kepple, W. Li, J. E. Dwyer, J. Matias, B. Baljinnyam, J. D. Oliver, N. Rajeevan, J. H. F. Pedra, S. Narasimhan, Y. Wang, U. Munderloh, E. Fikrig, A. Simeonov, J. Anguita, U. Pal, Dome1-JAK-STAT signaling between parasite and host integrates vector immunity and development. *Science* **379**, eabl3837 (2023).
25. D. Zhang, M. Li, S. Chen, H. Du, H. Zhong, J. Wu, F. Liu, Q. Zhang, F. Peng, X. Liu, K. W. K. Yeung, Novel palladium hydride surface enabling simultaneous bacterial killing and osteogenic formation through proton capturing and activation of antioxidant system in immune microenvironments. *Adv. Mater.* **36**, e2404485 (2024).
26. D. A. Fruman, C. Rommel, PI3K and cancer: Lessons, challenges and opportunities. *Nat. Rev. Drug Discov.* **13**, 140–156 (2014).
27. Y. Niu, Z. Wang, Y. Shi, L. Dong, C. Wang, Modulating macrophage activities to promote endogenous bone regeneration: Biological mechanisms and engineering approaches. *Bioact. Mater.* **6**, 244–261 (2021).
28. J. Muñoz, N. S. Akhavan, A. P. Mullins, B. H. Arjmandi, Macrophage polarization and osteoporosis: A review. *Nutrients* **12**, 2999 (2020).
29. B. N. Brown, S. F. Badylak, Expanded applications, shifting paradigms and an improved understanding of host-biomaterial interactions. *Acta Biomater.* **9**, 4948–4955 (2013).
30. F. A. Pinho-Ribeiro, W. A. Verri Jr., I. M. Chiu, Nociceptor sensory neuron-immune interactions in pain and inflammation. *Trends Immunol.* **38**, 5–19 (2017).
31. X. Fang, J. Wang, C. Ye, J. Lin, J. Ran, Z. Jia, J. Gong, Y. Zhang, J. Xiang, X. Lu, C. Xie, J. Liu, Polyphenol-mediated redox-active hydrogel with H_2S gaseous-bioelectric coupling for periodontal bone healing in diabetes. *Nat. Commun.* **15**, 9071 (2024).
32. Y. Li, X. Qu, B. Cao, T. Yang, Q. Bao, H. Yue, L. Zhang, G. Zhang, L. Wang, P. Qiu, N. Zhou, M. Yang, C. Mao, Selectively suppressing tumor angiogenesis for targeted breast cancer therapy by genetically engineered phage. *Adv. Mater.* **32**, e2001260 (2020).
33. D. Santos, F. Gonzalez-Perez, X. Navarro, J. Del Valle, Dose-dependent differential effect of neurotrophic factors on in vitro and in vivo regeneration of motor and sensory neurons. *Neural Plast.* **2016**, 4969523 (2016).
34. Z. Ye, J. Wei, C. Zhan, J. Hou, Role of transforming growth factor beta in peripheral nerve regeneration: Cellular and molecular mechanisms. *Front. Neurosci.* **16**, 917587 (2022).
35. K. I. Jeon, K. R. Huxlin, How scars shape the neural landscape: Key molecular mediators of TGF-β1's anti-neuritogenic effects. *PLOS ONE* **15**, e0234950 (2020).
36. L. Capossela, A. Gatto, S. Ferretti, L. Di Sarno, B. Graglia, M. Massese, M. Soligo, A. Chiaretti, Multifaceted roles of nerve growth factor: A comprehensive review with a special insight into pediatric perspectives. *Biology (Basel)* **13**, 546 (2024).
37. Z. Dang, E. Avolio, A. Albertario, G. B. Sala-Newby, A. C. Thomas, N. Wang, C. Emanueli, P. Madeddu, Nerve growth factor gene therapy improves bone marrow sensory innervation and nociceptor-mediated stem cell release in a mouse model of type 1 diabetes with limb ischaemia. *Diabetologia* **62**, 1297–1311 (2019).
38. B. L. Wise, M. F. Seidel, N. E. Lane, The evolution of nerve growth factor inhibition in clinical medicine. *Nat. Rev. Rheumatol.* **17**, 34–46 (2021).
39. Q. Q. Wan, W. P. Qin, Y. X. Ma, M. J. Shen, J. Li, Z. B. Zhang, J. H. Chen, F. R. Tay, L. N. Niu, K. Jiao, Crosstalk between bone and nerves within bone. *Adv. Sci. (Weinh)* **8**, 2003390 (2021).
40. S. Lee, C. Hwang, S. Marini, R. J. Tower, Q. Qin, S. Negri, C. A. Pagani, Y. Sun, D. M. Stepien, M. Sorkin, C. A. Kubiak, N. D. Visser, C. A. Meyers, Y. Wang, H. A. Rasheed, J. Xu, S. Miller, A. K. Huber, L. Minichiello, P. S. Cederna, S. W. P. Kemp, T. L. Clemens, A. W. James, B. Levi, NGF-TrkA signaling dictates neural ingrowth and aberrant osteochondral differentiation after soft tissue trauma. *Nat. Commun.* **12**, 4939 (2021).
41. M. Marcus, H. Skaat, N. Alon, S. Margel, O. Shefi, NGF-conjugated iron oxide nanoparticles promote differentiation and outgrowth of PC12 cells. *Nanoscale* **7**, 1058–1066 (2015).
42. Z. Okur, O. I. Senturk, C. Yilmaz, G. Gulseren, B. Mammadov, M. O. Guler, A. B. Tekinay, Promotion of neurite outgrowth by rationally designed NGF-β binding peptide nanofibers. *Biomater. Sci.* **6**, 1777–1790 (2018).
43. D. Ghosh, Y. Lee, S. Thomas, A. G. Kohli, D. S. Yun, A. M. Belcher, K. A. Kelly, M13-templated magnetic nanoparticles for targeted in vivo imaging of prostate cancer. *Nat. Nanotechnol.* **7**, 677–682 (2012).
44. X. Lv, F. Gao, X. Cao, Skeletal interoception in bone homeostasis and pain. *Cell Metab.* **34**, 1914–1931 (2022).
45. J. Yin, H. Hu, X. Li, M. Xue, W. Cheng, Y. Wang, Y. Xuan, X. Li, N. Yang, Y. Shi, S. Yan, Inhibition of Notch signaling pathway attenuates sympathetic hyperinnervation together with the augmentation of M2 macrophages in rats post-myocardial infarction. *Am. J. Physiol. Cell Physiol.* **310**, C41–C53 (2016).
46. M. Martínez-Casales, R. Hernanz, M. J. Alonso, Vascular and macrophage heme oxygenase-1 in hypertension: A mini-review. *Front. Physiol.* **12**, 643435 (2021).
47. T. Sono, C. A. Meyers, D. Miller, C. Ding, E. F. McCarthy, A. W. James, Overlapping features of rapidly progressive osteoarthrosis and Charcot arthropathy. *J. Orthop.* **16**, 260–264 (2019).
48. P. Manrique, B. Bolduc, S. T. Walk, J. van der Oost, W. M. de Vos, M. J. Young, Healthy human gut phageome. *Proc. Natl. Acad. Sci. U.S.A.* **113**, 10400–10405 (2016).
49. R. M. Dedrick, C. A. Guerrero-Bustamante, R. A. Garlena, D. A. Russell, K. Ford, K. Harris, K. C. Gilmour, J. Soothill, D. Jacobs-Sera, R. T. Schooley, G. F. Hatfull, H. Spencer, Engineered bacteriophages for treatment of a patient with a disseminated drug-resistant Mycobacterium abscessus. *Nat. Med.* **25**, 730–733 (2019).
50. S. Zhang, B. Hu, W. Liu, P. Wang, X. Lv, S. Chen, Z. Shao, The role of structure and function changes of sensory nervous system in intervertebral disc-related low back pain. *Osteoarthr. Cartil.* **29**, 17–27 (2021).
51. P. Laakkonen, K. Porkka, J. A. Hoffman, E. Ruoslahti, A tumor-homing peptide with a targeting specificity related to lymphatic vessels. *Nat. Med.* **8**, 751–755 (2002).
52. R. Ismail, N. D. Dorighello Carareto, J. C. Hornez, F. Bouchart, A localized phage-based antimicrobial system: Effect of alginate on phage desorption from β-TCP ceramic bone substitutes. *Antibiotics (Basel)* **9**, 560 (2020).
53. F. Bouchart, O. Vidal, J.-M. Lacroix, C. Spriet, S. Chamary, A. Brutel, J.-C. Hornez, 3D printed bioceramic for phage therapy against bone nosocomial infections. *Mater. Sci. Eng. C Mater. Biol. Appl.* **111**, 110840 (2020).
54. G. P. Smith, T. R. Gingrich, Hydroxyapatite chromatography of phage-display virions. *Biotechniques* **39**, 879–884 (2005).
55. M. Decodts, C. Cantallops-Vilà, J.-C. Hornez, J.-M. Lacroix, F. Bouchart, Phage-loaded biomimetic apatite powder with antibiofilm activity to treat bone-associated infections. *J. Biomed. Mater. Res. A* **113**, e37808 (2025).
56. S.-C. Tao, X.-R. Li, W.-J. Wei, Z.-Y. Wei, C.-R. Zhang, F. Wang, H. Dawes, S.-C. Guo, Polymeric coating on β-TCP scaffolds provides immobilization of small extracellular vesicles with surface-functionalization and ZEB1-Loading for bone defect repair in diabetes mellitus. *Biomaterials* **283**, 121465 (2022).
57. Z. Li, T. Du, C. Ruan, X. Niu, Bioinspired mineralized collagen scaffolds for bone tissue engineering. *Bioact. Mater.* **6**, 1491–1511 (2021).
58. D. Huang, K. Xu, X. Huang, N. Lin, Y. Ye, S. Lin, J. Zhang, J. Shao, S. Chen, M. Shi, X. Zhou, P. Lin, Y. Xue, C. Yu, X. Yu, Z. Ye, K. Cheng, Remotely temporal scheduled macrophage phenotypic transition enables optimized immunomodulatory bone regeneration. *Small* **18**, e2203680 (2022).
59. V. A. Kornev, E. A. Grebenik, A. B. Solovieva, R. I. Dmitriev, P. S. Timashev, Hydrogel-assisted neuroregeneration approaches towards brain injury therapy: A state-of-the-art review. *Comput. Struct. Biotechnol. J.* **16**, 488–502 (2018).
60. T. J. Koh, L. A. DiPietro, Inflammation and wound healing: The role of the macrophage. *Expert Rev. Mol. Med.* **13**, e23 (2011).

61. S. Dimmen, L. Nordsletten, J. E. Madsen, Parecoxib and indomethacin delay early fracture healing: A study in rats. *Clin. Orthop. Relat. Res.* **467**, 1992–1999 (2009).
62. X. Bai, W. Liu, L. Xu, Q. Ye, H. Zhou, C. Berg, H. Yuan, J. Li, W. Xia, Sequential macrophage transition facilitates endogenous bone regeneration induced by Zn-doped porous microcrystalline bioactive glass. *J. Mater. Chem. B* **9**, 2885–2898 (2021).
63. Z.-K. Zhang, X. Guo, J. Lao, Y.-X. Qin, Effect of capsaicin-sensitive sensory neurons on bone architecture and mechanical properties in the rat hindlimb suspension model. *J. Orthop. Translat.* **10**, 12–17 (2017).
64. C. Schlundt, T. El Khassawna, A. Serra, A. Dienelt, S. Wendler, H. Schell, N. van Rooijen, A. Radbruch, R. Lucius, S. Hartmann, G. N. Duda, K. Schmidt-Bleek, Macrophages in bone fracture healing: Their essential role in endochondral ossification. *Bone* **106**, 78–89 (2018).
65. J.-X. Duan, Y. Zhou, A.-Y. Zhou, X.-X. Guan, T. Liu, H.-H. Yang, H. Xie, P. Chen, Calcitonin gene-related peptide exerts anti-inflammatory property through regulating murine macrophages polarization in vitro. *Mol. Immunol.* **91**, 105–113 (2017).
66. M. Li, X. Zhong, W. Xu, Substance P increases STAT6-mediated transcription activation of lymphocyte cytosolic protein 2 to sustain M2 macrophage predominance in pediatric asthma. *Am. J. Pathol.* **194**, 238–252 (2024).
67. J. Rodrigo, J. M. Polak, G. Terenghi, C. Cervantes, M. A. Ghatei, P. K. Mulderry, S. R. Bloom, Calcitonin gene-related peptide (CGRP)-immunoreactive sensory and motor nerves of the mammalian palate. *Histochemistry* **82**, 67–74 (1985).
68. M. Risch, B. Vogler, M. Dux, K. Messlinger, CGRP outflow into jugular blood and cerebrospinal fluid and permeance for CGRP of rat dura mater. *J. Headache Pain* **22**, 105 (2021).
69. K. Yuan, J. Zheng, X. Shen, Y. Wu, Y. Han, X. Jin, X. Huang, Sensory nerves promote corneal inflammation resolution via CGRP mediated transformation of macrophages to the M2 phenotype through the PI3K/AKT signaling pathway. *Int. Immunopharmacol.* **102**, 108426 (2022).
70. S. G. Grässel, The role of peripheral nerve fibers and their neurotransmitters in cartilage and bone physiology and pathophysiology. *Arthritis Res. Ther.* **16**, 485 (2014).
71. T. Fukuda, S. Takeda, R. Xu, H. Ochi, S. Sunamura, T. Sato, S. Shibata, Y. Yoshida, Z. Gu, A. Kimura, C. Ma, C. Xu, W. Bando, K. Fujita, K. Shinomiya, T. Hirai, Y. Asou, M. Enomoto, H. Okano, A. Okawa, H. Itoh, Sema3A regulates bone-mass accrual through sensory innervations. *Nature* **497**, 490–493 (2013).
72. Q. Qiu, X. Yu, Q. Chen, X. He, Sema3A inactivates the ERK/JNK signalling pathways to alleviate inflammation and oxidative stress in lipopolysaccharide-stimulated rat endothelial cells and lung tissues. *Autoimmunity* **56**, 2200908 (2023).
73. M. Rienks, P. Carai, N. Bitsch, M. Schellings, M. Vanhaverbeke, J. Verjans, I. Cuijpers, S. Heymans, A. Papageorgiou, Sema3A promotes the resolution of cardiac inflammation after myocardial infarction. *Basic Res. Cardiol.* **112**, 42 (2017).
74. Y. Han, X. You, W. Xing, Z. Zhang, W. Zou, Paracrine and endocrine actions of bone-the functions of secretory proteins from osteoblasts, osteocytes, and osteoclasts. *Bone Res.* **6**, 16 (2018).
75. K. Wu, D. Huang, X. Huang, The effects of semaphorin 3A in bone and cartilage metabolism: Fundamental mechanism and clinical potential. *Front. Cell Dev. Biol.* **11**, 1321151 (2023).
76. P. J. Jost, D. Vucic, Regulation of cell death and immunity by XIAP. *Cold Spring Harb. Perspect. Biol.* **12**, a036426 (2020).
77. M. Daoud, P. N. Broxtermann, F. Schorn, J. P. Werthenbach, J. M. Seeger, L. M. Schiffmann, K. Brinkmann, D. Vucic, T. Tüting, C. Mauch, D. Kulms, P. Zigrino, H. Kashkar, XIAP promotes melanoma growth by inducing tumour neutrophil infiltration. *EMBO Rep.* **23**, e53608 (2022).
78. T. Goncharov, S. Hedayati, M. M. Mulvihill, A. Izrael-Tomasevic, K. Zobel, S. Jeet, A. V. Fedorova, C. Eidenschenk, J. deVoss, K. Yu, A. S. Shaw, D. S. Kirkpatrick, W. J. Fairbrother, K. Deshayes, D. Vucic, Disruption of XIAP-RIP2 association blocks NOD2-mediated inflammatory signaling. *Mol. Cell* **69**, 551–565.e7 (2018).
79. N. Osumi, H. Shinohara, K. Numayama-Tsuruta, M. Maekawa, Concise review: Pax6 transcription factor contributes to both embryonic and adult neurogenesis as a multifunctional regulator. *Stem Cells* **26**, 1663–1672 (2008).
80. T. Pfirrmann, E. Jandt, S. Ranft, A. Lokapally, H. Neuhaus, M. Perron, T. Hollemann, Hedgehog-dependent E3-ligase Midline1 regulates ubiquitin-mediated proteasomal degradation of Pax6 during visual system development. *Proc. Natl. Acad. Sci. U.S.A.* **113**, 10103–10108 (2016).
81. W. Hu, X. Yu, Z. Liu, Y. Sun, X. Chen, X. Yang, X. Li, W. K. Lam, Y. Duan, X. Cao, H. Steller, K. Liu, P. Huang, The complex of TRIP-Br1 and XIAP ubiquitinates and degrades multiple adenylyl cyclase isoforms. *eLife* **6**, e28021 (2017).
82. S. Mishra, S. K. Maurya, K. Srivastava, S. Shukla, R. Mishra, Pax6 influences expression patterns of genes involved in neuro-degeneration. *Ann. Neurosci.* **22**, 226–231 (2015).
83. S. K. Maurya, R. Mishra, Pax6 interacts with Iba1 and shows age-associated alterations in brain of aging mice. *J. Chem. Neuroanat.* **82**, 60–64 (2017).
84. T. Tian, L. Chen, Z. Wang, M. Zhu, W. Xu, B. Wu, Sema3A drives alternative macrophage activation in the resolution of periodontitis via PI3K/AKT/mTOR Signaling. *Inflammation* **46**, 876–891 (2023).
85. W. Yang, S. Yang, F. Zhang, F. Cheng, X. Wang, J. Rao, Influence of the Hippo-YAP signalling pathway on tumor associated macrophages (TAMs) and its implications on cancer immunosuppressive microenvironment. *Ann. Transl. Med.* **8**, 399 (2020).
86. Y. Yuan, D. Wu, Y. Hou, Y. Zhang, C. Tan, X. Nie, Z. Zhao, J. Hou, Wnt signaling: Modulating tumor-associated macrophages and related immunotherapeutic insights. *Biochem. Pharmacol.* **223**, 116154 (2024).
87. Y. Wu, D. Jing, H. Ouyang, L. Li, M. Zhai, Y. Li, L. Bi, P. Guoxian, Pre-implanted sensory nerve could enhance the neurotization in tissue-engineered bone graft. *Tissue Eng. Part A* **21**, 2241–2249 (2015).

Acknowledgments: We thank Y. Peng from the Department of Orthopaedics, Union Hospital, Tongji Medical College, Huazhong University of Science and Technology; J. Chen and Q. Huang from the core facility platform of Zhejiang University School of Medicine; and X. Li from the Center for Basic and Translational Research, The Second Affiliated Hospital of Zhejiang University for technical supports. **Funding:** This study was supported by the National Natural Science Foundation of China (82372382) (X.H.); National Natural Science Foundation of China (8200233) (D.H.); National Natural Science Foundation of China (32371412 and 32071349) and Zhejiang Provincial Natural Science Foundation of China (LY24C100001) (J.X.); and Central Guidance on Local Science and Technology Development Fund of Zhejiang Province (2024ZY01033) and the Key Research and Development Program of Zhejiang (no. 2022C01076) (Z.Y.). **Author contributions:** Conceptualization: K.X., L.C., H.L., J.X., D.H., and X.H. Methodology: K.X., K.W., L.C., D.H., and X.H. Software: K.X. and K.W. Investigation: K.X., K.W., Y.Z., H.L., N.L., and X.H. Formal analysis: K.X., K.W., Y.Z., H.L., N.L., and X.H. Software: K.X. and K.W. Data curation: K.X. and K.W. Visualization: K.X., K.W., L.C., and J.X. Resources: K.X., Z.Y., and X.H. Validation: K.X., K.W., L.C., H.L., J.X., and D.H. Supervision: K.X., H.L., J.X., and X.H. Project administration: K.X., Z.Y., J.X., and X.H. Funding acquisition: D.H., Z.Y., J.X., and X.H. Writing—original draft: K.X., L.C., and D.H. Writing—review and editing: K.X., L.C., H.L., Z.Y., J.X., D.H., and X.H. **Competing interests:** The authors declare that they have no competing interests. **Data and materials availability:** All data needed to evaluate the conclusions in the paper are present in the paper and/or the Supplementary Materials.

Submitted 5 September 2024
Accepted 14 February 2025
Published 21 March 2025
10.1126/sciadv.ads9581